A UNIFIED VARIATIONAL FRAMEWORK ON MACROSCOPIC COMPUTATIONS FOR TWO-PHASE FLOW WITH MOVING CONTACT LINES*

XIANMIN XU †

Abstract. Two-phase flow with moving contact lines is an unsolved problem in fluid dynamics. It is challenging to solve the problem numerically due to its intrinsic multiscale nature that the microscopic slipness must be taken into account in a macroscopic model. It is even more difficult when the solid substrate has microscopically inhomogeneity or roughness. In this paper, we propose a novel unified numerical framework for two-phase flows with moving contact lines. The framework cover some typical sharp-interface models for moving contact lines and can deal with the contact angle hysteresis(CAH) naturally. We prove that all the models, including the nonlinear Cox model and a CAH model, are thermodynamically consistent in the sense that an energy dissipation relation is satisfied. We further derive a new variational formula which leads to a stable and consistent numerical method independent of the choice of the slip length and the contact line frictions. This enables us to solve efficiently the macroscopic models for moving contact lines without resolving very small scale in the vicinity of the contact line. We prove the well-posedness of the fully decoupled scheme which is based on a stabilized extended finite element discretization and a level-set representation for the free interface. Numerical examples are given to show the efficiency of the numerical framework.

1. Introduction. A contact line in two-phase flow is the intersection of the two-fluid interface with the solid boundary. Two-phase flow with moving contact lines(MCLs) is very common in nature and our daily life, such as in wetting, printing, coating, etc. Modeling and numerical simulations for the moving contact line problem are very challenging due to its intrinsic multiscale property [1, 2]. It is known that the microscopic slipness near the moving contact line must be taken into account in a macroscopic continuum model. Otherwise, the standard no slip boundary condition may lead to infinite energy dissipations [3]. The is referred to as contact line paradox in literature. In addition, microscopic inhomogeneity of the solid surface may induce the phenomena of contact angle hysteresis [4, 5, 6]. This makes solving the two-phase problem with MCLs very difficult in real applications.

To avoid the contact line paradox, there exist many models in literature (c.f. [7, 8, 9, 10]). One simple way is to use the Navier slip boundary condition instead of the no-slip boundary condition and to assume that the microscopic contact angle is equal to the equilibrium Young's angle [7] . By molecular dynamics simulations, Qian *et al* found that the microscopic dynamic contact angle can be different from the static one and they proposed a phase-field model with a generalized Navier slip boundary condition [11, 12]. A sharp interface model is proposed by Ren & E [13, 14], which is also consistent with molecular dynamics simulations. Other widely used boundary conditions for MCLs include the model based on the molecular kinetic theory [15], the surface generation model [16, 17], and the phase-field models with effective slipness [18, 19].

All the above-mentioned models are microscopic models in the sense that they describes behavior of the contact angle in a microscopic scale. The models include some microscopic parameters, such as the slip length, the molecular adhesive parameter, etc. To solve such models numerically, usually one needs to choose triangulations with mesh size smaller than the microscopic parameters to get reasonable approximations. In general, it is very expensive to quantitatively simulate a problem with

*The work was partially supported by NSFC 11971469.

† LSEC, ICMSEC, NCMIS, Academy of Mathematics and Systems Science, Chinese Academy of Sciences, Beijing 100190, China, xmxu@lsec.cc.ac.cn

a macroscopic size. Therefore, most previous numerical studies for the microscopic models are for problems with very small size or to present qualitative simulations in the sense that some parameters are chosen artificially [20, 21, 22, 23, 24, 25, 26, 27].

To solve the MCL problem with macroscopic size, Sui & Spelt developed numerical methods for a macroscopic model on homogeneous surfaces [28, 29]. They adopt the boundary conditions proposed by Cox [30, 31]. The Cox model gives a nonlinear relation between the apparent contact angle in macroscopic scale and the velocity of contact line motion. In [28, 29], the authors use a finite difference method to discretize the partial differential equations and choose mesh dependent parameters in Cox's model. Numerical examples show that the method gives results consistent with physical experiments. Mesh depedent models have also been studied in a volume of fluid method [32]. Numerical simulations for three dimensional problems are presented in [33].

For two-phase flow problems with contact angle hysteresis, there is relatively few numerical work in literature(c.f [21, 34, 33, 35, 36]). Most previous work assumes that the advancing and receding contact angle are known a priori. In simulations, the contact line velocity is set to be zero if the contact angle is in the interval $[\theta_r, \theta_a]$. Very recently, Yue developed efficient methods for two-phase flow problems with CAH [35, 36]. They proposed a phase field model and a level-set model, both of which guarantee the CAH condition automatically.

Recently, some new macroscopic models are developed for MCLs on both homogeneous and chemically patterned surfaces [37, 38]. The derivation of the models are based on a model reduction method by the Onsager principle and a multiscale analysis for the reduced dynamic system for problems with periodic inhomogeneity on solid surface. The boundary conditions give quantitative relations between the apparent contact angle, the contact line velocity and the local chemical property of the substrate near the contact line. It is found that the boundary condition on homogeneous substrates is a first order approximation to the standard Cox boundary condition when the capillary number is small. The boundary condition on inhomogeneous substrates explains very well the experimental results on dynamic contact angle hysteresis in [39, 40].

In this paper, we present studies on numerical methods for two-phase flow with MCLs. We first develop a unified mathematical framework which can handle many sharp interface models, such as the Ren-E model, the Cox model, the Onsager model and the CAH model. We show that all the models are thermodynamically consistent in the sense that an energy dissipation relation is satisfied. As far as we know, this is new for the Cox model and the CAH model, where the boundary conditions need a transformation. Motivated by the work [41, 42], we further derive a new variational formula, which can handle the unbounded parameters in the MCL models efficiently. This enables us to develop a finite element method which is stable independent of the choice of slip length and the contact line friction coefficient.We prove an inf-sup inequality and the well-posedness for the fully discrete problem. Numerical experiments are given to show the efficiency of the method and to compare various models. It turns out that the method has nice convergence property even on triangulations with mesh size larger than the slip length. The two-phase problem with contact angle hysteresis can also be solved efficiently.

The rest of the paper is organized as follows. In section 2, we introduce several sharp interface models, including the Ren-E model, the Cox model, the Onsager model and a model for CAH. We reformulate them into a unified form. We proved that all the models are thermodynamically consistent. In section 3, we derived a variational formula for the MCL problem. In the variational problem, we impose the boundary condition weakly by a Nitsche technique and use a rescaling technique to ensure the coefficient in the variational formula bounded away from infinity. In section 4, we introduce the finite element discretization to the variational problem by using the XFEM for the discrete pressure and the level-set method capturing the free interface. In section 5, we show the well-posedness of the fully decoupled problem by proving a discrete inf-sup condition. Numerical examples are shown in section 6 to verify the efficiency of the method and to compare different models. Some conclusion remarks are given in section 7.

2. A mathematical framework.

In this section, we introduce some continuum models for moving contact lines, including one for contact angle hysteresis which is proposed recently in [37]. We will reformulate them into a unified form. We show that all the models are thermodynamically consistent in the sense that they satisfies an energy dissipation relation. However, the friction coefficient can be unbounded in some situations, especially for the model with contact angle hysteresis.

2.1. The fluid equation.

Suppose a domain $\Omega = \Omega_1 \cup \Omega_2 \subset \mathbb{R}^3$ is occupied by two immiscible fluids. Away from the moving contact line, the viscous fluids can be described by a system of impressible Navier-Stokes equations,

$$\begin{cases} \rho_i \left(\frac{\partial \boldsymbol{u}}{\partial t} + \boldsymbol{u} \cdot \nabla \boldsymbol{u} \right) = \mathbf{div} \boldsymbol{\sigma}_i + \rho_i \boldsymbol{g}, & \text{in } \Omega_i(t), \\ \nabla \cdot \boldsymbol{u} = 0, & \text{in } \Omega_i(t), \end{cases} \tag{2.1}$$

where $\boldsymbol{u}$ is the velocity of the fluids, $\rho_i (i = 1, 2)$ is the density, $\boldsymbol{g}$ is the gravitational acceleration, and $\boldsymbol{\sigma}_i$ is the stress. For viscous fluids, we have

$$\boldsymbol{\sigma}_i := -p\mathbf{I} + \mu_i \mathbf{D}(\boldsymbol{u}),$$

where μ_i is the viscous coefficient, $\mathbf{D}(\boldsymbol{u}) := \nabla \boldsymbol{u} + (\nabla \boldsymbol{u})^T$, and p is the pressure. Denote by $\Gamma(t) = \partial\Omega_1 \cup \partial\Omega_2$ the interface between the two fluid regions. On the interface we have the standard interface conditions,

$$[\boldsymbol{\sigma} \boldsymbol{n}_\Gamma] = -\gamma \kappa \boldsymbol{n}_\Gamma, \quad [\boldsymbol{u}] = 0, \quad V_\Gamma = \boldsymbol{u} \cdot \boldsymbol{n}_\Gamma, \qquad \text{on } \Gamma(t). \tag{2.2}$$

The first equality in (2.2) means balance of the stress across the interface, where $[\boldsymbol{\sigma} \boldsymbol{n}_\Gamma] := (\boldsymbol{\sigma}_1 - \boldsymbol{\sigma}_2) \boldsymbol{n}_\Gamma$, $\boldsymbol{n}_\Gamma$ is the unit normal of $\Gamma(t)$ pointing into Ω_2, γ is the surface tension and κ is the mean curvature of the interface. Notice that $[\mathbf{u}] := \mathbf{u}_1 - \mathbf{u}_2$ is the jump of the fluid velocity and V_Γ is the velocity of the interface. The other two equations in (2.2) imply that the fluid velocity is continuous across the interface and the interface evolves with the normal velocity of the fluid.

Suppose a part of the boundary of Ω is solid surface which is denoted as Γ_S. On the solid surface we use the Navier slip boundary condition for both fluids,

$$\boldsymbol{u} \cdot \boldsymbol{n}_S = 0, \quad \beta_i \mathbf{P}_S \boldsymbol{u} = -\mathbf{P}_S \boldsymbol{\sigma}_i \boldsymbol{n}_S, \qquad \text{on } \Gamma_S, \tag{2.3}$$

where $\boldsymbol{n}_S$ is the unit out normal of Γ_{S}, $\mathbf{P}_S = \mathbf{I} - \boldsymbol{n}_S \boldsymbol{n}_S^T$ is the projection operator which maps a vector to the tangential surface of Γ_{S}, β_i is an phenomenological coefficient and $l_{s,i} = \frac{\mu_i}{\beta_i}$ denotes the slip length, which is of nanoscale in general. One can easily show that

$$\mathbf{P}_S \boldsymbol{\sigma}_i \boldsymbol{n}_S = \mu_i \mathbf{P}_S \mathbf{D}(\boldsymbol{u}) \boldsymbol{n}_S =: S(\boldsymbol{u}, \boldsymbol{n}_S),$$

which represents the shear stress on the solid surface.

On the rest part of the boundary $\partial\Omega$, other boundary conditions should be chosen accordingly. For example, inflow and outflow conditions may be used in the parts where the fluids moves in or out of the domain. For simplicity, we suppose that $\boldsymbol{u} = 0$ on $\partial\Omega \setminus \Gamma_S$ in this paper.

When the two-phase interface $\Gamma(t)$ does not intersect with the solid boundary Γ_S, the above equations compose a complete system. Otherwise, when there is a contact line $L(t) = \Gamma(t) \cap \Gamma_S$, one needs extra conditions for MCLs to complete the model.

2.2. Boundary conditions for MCLs. In the following, we introduce several boundary conditions associated with the motion of contact lines. All of them can be coupled with the sharp interface two-phase flow equations described above.

The Ren-E model. A typical model for moving contact lines is proposed by Ren & E [14], which reads

$$\xi_m u_L = \gamma(\cos\theta_Y - \cos\theta_a). \tag{2.4}$$

Here θ_Y is the Young's angle, θ_a is the microscopic dynamic contact angle, and $\xi_m > 0$ is the contact line friction coefficient. u_L denotes the contact line velocity, which is in the normal direction of the contact line $L(t)$ in the tangential surface of Γ_S. In general, ξ_m might be quite small since it accounts to the friction of the contact line [43]. In principle, we could solve the equations (2.1)-(2.4) to simulate a moving contact line problem. However, it is usually very challenging to do this for a problem with macroscopic size. The reason is that one needs to use very fine meshes which is smaller than the slip length l_s (of nanoscale) [26].

The Cox model. To avoid using too fine meshes near the contact line, we can consider some macroscopic models as in [28]. The first macroscopic model is the well-known boundary condition by Cox, which is derived by delicate asymptotic analysis [30]. The condition reads

$$\mu_1 |\ln\zeta| u_L = \gamma(\mathcal{G}(\theta_a,\lambda) - \mathcal{G}(\theta_Y,\lambda)), \tag{2.5}$$

where θ_a is the apparent contact angle on a mesoscale l, $\zeta = \frac{l}{l_s}$ is the ratio between l and the slip length l_s and $\lambda = \frac{\mu_2}{\mu_1}$ is the ratio between the viscosity of the two fluids. Here the nonlinear function

$$\mathcal{G}(\theta,\lambda) = \int_0^\theta \mathcal{F}(\alpha,\lambda)\sin\alpha d\alpha,$$

with

$$\mathcal{F}(\alpha,\lambda) = \frac{\lambda(\alpha^2 - \sin^2\alpha)(\pi - \alpha + \cos\alpha\sin\alpha) + ((\pi-\alpha)^2 - \sin^2\alpha)(\alpha - \cos\alpha\sin\alpha)}{2\sin^2\alpha(\lambda^2(\alpha^2 - \sin^2\alpha) + 2\lambda(\sin^2\alpha + \alpha(\pi-\alpha)) + ((\pi-\alpha)^2 - \sin^2\alpha))}.$$

For later applications, we will rewrite Cox's model into a different form as follows,

$$\xi_{cox}(\theta_a) u_L = \gamma(\cos\theta_Y - \cos\theta_a), \tag{2.6}$$

where $\xi_{cox}(\theta_a) = \frac{\mu_1|\ln\zeta|(\cos\theta_Y - \cos\theta_a)}{(\mathcal{G}(\theta_a,\lambda) - \mathcal{G}(\theta_Y,\lambda))}$ and

$$\xi_{cox}(\theta_Y) = \lim_{\theta_a \to \theta_Y} \frac{\mu_1|\ln\zeta|(\cos\theta_Y - \cos\theta_a)}{(\mathcal{G}(\theta_a,\lambda) - \mathcal{G}(\theta_Y,\lambda))} = \frac{\mu_1|\ln\zeta|}{\mathcal{F}(\theta_Y,\lambda)}.$$

It is easy to check that $\xi_{cox}(\theta_a)$ is a continuous function in the above definition. Later we will show that $\xi_{cox}(\theta_a)$ is always positive so that the Cox boundary condition will lead to a thermodynamically consistent system.

A model derived from the Onsager principle. The second macroscopic model is that derived recently by using the Onsager principle as an approximation tool [37]. The boundary condition reads

$$\xi_{ons}(\theta_a)u_L = \gamma(\cos\theta_Y - \cos\theta_a), \tag{2.7}$$

where $\xi_{ons}(\theta_a) = \left(\xi_m + \frac{\mu_1 |\ln\zeta|}{\mathcal{F}(\theta_a,\lambda)}\right)$. One can see that the equation is a first order approximation to the Cox model (2.6) when the capillary number $Ca := \mu u_L/\gamma$ is small and ξ_m in the coefficient ξ_{ons} is negligible.

To use the macroscopic models in a numerical method, the resolution near the contact line is characterized by the local mesh size h. Therefore, we set h as the characteristic mesoscopic length where the apparent contact angle is defined. In this case, we choose $\zeta = \frac{h}{l_s}$ in our numerical method in this paper. Similar techniques have been used in [32, 28].

A coarse-grained model for contact angle hysteresis. When the solid surface is inhomogeneous, the apparent advancing angle is different from the receding one. This is referred to as contact angle hysteresis. A coarse-grained model for CAH is developed recently in [37]. For simplicity, we assume that $\theta_Y(x,z)$ is a smooth function which depends on a fast variable z in the normal direction of the contact line. For any given x, we suppose that $\theta_Y(x,z)$ is a periodic function of z with period ϵ, and $\theta_1 = \min_z \theta_Y(x,z)$, $\theta_2 = \max_z \theta_Y(x,z)$ with $\theta_i \in (0,\pi)$. In this case, the averaged model reads,

$$\xi_{ons}(\theta_a)u_L = \gamma\left(\frac{1}{\epsilon}\int_0^\epsilon \frac{dz}{\cos\theta_Y(x,z) - \cos\theta_a}\right)^{-1}, \qquad x \in \Gamma_S. \tag{2.8}$$

Here θ_a is the time averaged contact angle. The formula describes the contact angle hysteresis naturally. It can be verified that when u_L goes to zero, the advancing contact angle approaches to θ_2 and the receding one approaches to θ_1 [37].

For the purpose of numerical simulations, we rewrite the boundary condition into an equivalent form,

$$\tilde{\xi}_{hys}(\theta_a)u_L = \gamma\left(\frac{1}{\epsilon}\int_0^\epsilon \cos\theta_Y(x,z)dz - \cos\theta_a\right), \tag{2.9}$$

where

$$\tilde{\xi}_{hys}(\theta) = \begin{cases} \xi_{ons}(\theta)\left(\frac{1}{\epsilon}\int_0^\epsilon \cos\theta_Y(x,z)dz - \cos\theta\right)\left(\frac{1}{\epsilon}\int_0^\epsilon \frac{dz}{\cos\theta_Y(x,z)-\cos\theta}\right), & \text{if } \theta \notin [\theta_1,\theta_2], \\ +\infty, & \text{if } \theta \in [\theta_1,\theta_2]. \end{cases}$$

In the above definition, $\tilde{\xi}_{hys}(\theta_a)$ can be equal to infinity when the contact angle is in the interval of the receding contact angle and advancing angle since the integral $\frac{1}{\epsilon}\int_0^\epsilon \frac{dz}{\cos\theta_Y(x,z)-\cos\theta}$ diverges when $\theta \in [\theta_1,\theta_2]$. This means the contact line is pinned there, i.e. $u_L = 0$. To avoid using the infinity in numerical simulations, we use

$$\xi_{hys}(\theta_a) = \min(\tilde{\xi}_{hys}(\theta_a), \xi_\infty), \tag{2.10}$$

instead of $\tilde{\xi}_{hys}$ in (2.9) with $\xi_\infty \gg 0$ being a large regularized parameter. The coarse-grained model for CAH reads

$$\xi_{hys}(\theta_a)u_L = \gamma\left(\frac{1}{\epsilon}\int_0^\epsilon \cos\theta_Y(x,z)dz - \cos\theta_a\right). \tag{2.11}$$

Table 1: Choice of the parameters for different models.

Model	β_L	$\psi(\theta_Y)$
Ren-E	ξ_m	$\cos\theta_Y$
Cox	ξ_{cox}	$\cos\theta_Y$
Onsager	ξ_{ong}	$\cos\theta_Y$
CAH	ξ_{hys}	$\frac{1}{\epsilon}\int_0^\epsilon \cos\theta_Y d\zeta$

Finally, we can write all the above models into a unified form,

$$\beta_L u_L = \gamma(\psi(\theta_Y) - \cos\theta_a), \tag{2.12}$$

where the choice of the parameters β_L and $\psi(\theta_Y)$ are listed in Table 1 for various models. We will propose a numerical framework for the general problem.

2.3. Energy dissipation relations. We first show that all the friction coefficients are positive. The conclusion is trivial for the Ren-E model. The following proposition presents results for the other models.

PROPOSITION 2.1. *Suppose $\theta_a \in (0,\pi)$, $\mu_1 > 0$ and $\lambda \geq 0$. Then all the coefficients ξ_{ons}, ξ_{cox}, ξ_{hys} in the previous macroscopic models are positive. Furthermore, the coefficients may approach to zero or infinity in different situations.*

Proof. We first consider ξ_{ons}. From the formula of $\mathcal{F}(\theta,\lambda)$, we could see that all the terms in $\mathcal{F}(\theta,\lambda)$ are positive when $\theta \in (0,\pi)$. For example, it is easy to verify that $\theta^2 - \sin^2\theta > 0$, $\pi - \theta + \cos\theta\sin\theta > 0$, $(\pi-\theta)^2 - \sin^2\theta > 0$ and $\theta - \cos\theta\sin\theta > 0$ when $\theta \in (0,\pi)$. This implies that $\mathcal{F}(\theta,\lambda)$ is a positive number and so is $\mathcal{F}(\theta,\lambda)^{-1}$. This simply implies that $\xi_{ons} > 0$. We then show that ξ_{ons} can approach to zero and infinity in various situations. In the first case, direct calculations show that $\lim_{\theta\to 0}\mathcal{F}(\theta,\lambda) = 0$. This indicates $\lim_{\theta\to 0}\xi_{ons} = \infty$. Next if we set $\lambda = 0$ and take θ goes to π, we can get $\lim_{\theta\to\pi}\mathcal{F}(\theta,0) = \infty$. This implies that ξ_{ons} goes to zero if $\xi_m = 0$.

We then consider ξ_{cox}. By the formula of $\mathcal{G}(\theta,\lambda)$, we know that $\frac{d\mathcal{G}(\theta,\lambda)}{d\theta} = \mathcal{F}(\theta,\lambda)\sin\theta > 0$ when $\theta \in (0,\pi)$. Therefore $\mathcal{G}(\theta,\lambda)$ is a monotonously increasing function with respect to θ in $(0,\pi)$. Notice that $\cos\theta$ is monotonously deceasing with respect to θ in $(0,\pi)$. We can easily see that $\frac{(\cos\theta_Y - \cos\theta_a)}{(\mathcal{G}(\theta_a,\lambda)-\mathcal{G}(\theta_Y,\lambda))} > 0$ whenever $\theta_a \neq \theta_Y$. Notice again $\lim_{\theta_a\to\theta_Y}\frac{(\cos\theta_Y-\cos\theta_a)}{(\mathcal{G}(\theta_a,\lambda)-\mathcal{G}(\theta_Y,\lambda))} = \frac{1}{\mathcal{F}(\theta_Y,\lambda)} > 0$. We see that ξ_{cox} is always positive. By the above analysis for $\mathcal{F}(\theta_Y,\lambda)$, we also know that ξ_{cox} can also approach to zero and infinity in different situations.

We now consider ξ_{hys}. We need only to analyze the value of the term

$$I(\theta_a, x) := \left(\frac{1}{\epsilon}\int_0^\epsilon \cos\theta_Y(x,z) - \cos\theta_a dz\right)\left(\frac{1}{\epsilon}\int_0^\epsilon \frac{dz}{\cos\theta_Y(x,z) - \cos\theta_a}\right).$$

Notice that $\cos\theta_1 \geq \frac{1}{\epsilon}\int_0^\epsilon \cos\theta_Y(x,z)dz \geq \cos\theta_2$. It is easy to see that both terms in $I(\theta_a,x)$ have the same sign when $\theta_a \notin [\theta_1,\theta_2]$ with $\theta_1,\theta_2 \in (0,\pi)$ being the lower and upper bound of the smooth function $\theta_Y(x,\cdot)$ in one period. This leads to $I(\theta_a,x) > 0$ when $\theta_a \notin [\theta_1,\theta_2]$. By the definition of ξ_{hys}, we can easily see that $\xi_{hys} > 0$, for all $\theta_a \in (0,\pi)$. We could also see that $\lim_{\theta_a\to\theta_1^-} I(\theta_a,x) = \lim_{\theta_a\to\theta_2^+} I(\theta_a,x) = +\infty$.

Therefore, ξ_{hys} approaches to infinity when the regularized parameter ξ_∞ goes to infinity. ∎

Proposition 2.1 shows that the friction coefficients in the above models are all positive. This enables us to show the energy dissipation relation for all the above models for MCLs. However, the unboundedness of the friction coefficients may cause troubles in numerical simulations.

For models without CAH, the total potential energy in the system is given as

$$\mathcal{E}_p = \int_{\Gamma_{S1}} \gamma_{S1} ds + \int_{\Gamma_{S2}} \gamma_{S2} ds + \int_{\Gamma} \gamma ds - \int_{\Omega} \rho \boldsymbol{g} \cdot \boldsymbol{x} dx, \tag{2.13}$$

where γ_{S1} and γ_{S2} denote the solid-fluid interface energy densities, $\Gamma_{S1} = \Gamma_S \cap \partial\Omega_1$ and $\Gamma_{S2} = \Gamma_S \cap \partial\Omega_2$. By the Young's equation, we have the relation

$$\gamma \cos\theta_Y = \gamma_{S2} - \gamma_{S1}.$$

The kinetic energy is defined as

$$\mathcal{E}_k = \int_\Omega \frac{\rho}{2} |\boldsymbol{u}|^2 dx. \tag{2.14}$$

We also define the energy dissipation functional

$$\Phi = \int_\Omega \frac{\mu}{4} |\mathbf{D}(\boldsymbol{u})|^2 dx + \int_{\Gamma_S} \frac{\beta_S}{2} |\mathbf{P}_S \boldsymbol{u}|^2 ds + \int_L \frac{\beta_L}{2} u_L^2 ds, \tag{2.15}$$

where β_L corresponds to ξ_m , ξ_{ons} or ξ_{cox} for different contact line models.

The following energy dissipation relation can be derived for the solution of the problem (2.1)-(2.3) coupled with one MCL model on homogeneous surfaces.

Proposition 2.2. *Let* $(\boldsymbol{u}, p)$ *be the solution of* (2.1)-(2.3) *coupled with one contact line model* (2.4), (2.6) *or* (2.7), *we have*

$$\frac{d}{dt}(\mathcal{E}_p + \mathcal{E}_k) = -2\Phi.$$

Proof. The proof of the proposition is standard. We briefly state the main steps for convenience of the readers. Firstly, the time derivative of the potential energy can be calculated as

$$\begin{aligned}\frac{d}{dt}\mathcal{E}_p &= \int_{L(t)} (\gamma_{S1} - \gamma_{S2}) u_L ds + \int_{L(t)} \cos\theta_a u_L \mathbf{ds} + \gamma \int_{\Gamma(t)} \kappa V_\Gamma ds - \int_\Omega \rho \boldsymbol{g} \cdot \boldsymbol{u} dx \\ &= \int_{L(t)} (\cos\theta_a - \cos\theta_Y) u_L ds + \gamma \int_{\Gamma(t)} \kappa V_\Gamma ds - \int_\Omega \rho \boldsymbol{g} \cdot \boldsymbol{u} dx.\end{aligned}$$

By the boundary conditions (2.4), (2.6) or (2.7), this leads to

$$\frac{d}{dt}\mathcal{E}_p = -\int_{L(t)} \beta_L u_L^2 ds + \gamma \int_{\Gamma(t)} \kappa V_\Gamma ds - \int_\Omega \rho \boldsymbol{g} \cdot \boldsymbol{u} dx, \tag{2.16}$$

where $\beta_L = \xi_m$, ξ_{cox} or ξ_{ons} respectively for different models.

The time derivative of the kinetic energy is

$$\frac{d}{dt}\mathcal{E}_k = \int_\Omega \frac{\partial \boldsymbol{u}}{\partial t} \cdot \boldsymbol{u} + (\boldsymbol{u} \cdot \nabla \boldsymbol{u}) \cdot \boldsymbol{u} dx.$$

By the equation (2.1), this leads to

$$
\begin{aligned}
\frac{d}{dt}\mathcal{E}_k &= \sum_{i=1}^{2}\int_{\Omega_i}(\mathbf{div}\boldsymbol{\sigma}_i+\rho_{\boldsymbol{i}}\boldsymbol{g})\cdot\boldsymbol{u}dx \\
&= \sum_{i=1}^{2}\left\{\int_{\partial\Omega_i}(\boldsymbol{\sigma}_i\boldsymbol{n})\cdot\boldsymbol{u}ds-\int_{\Omega_i}\boldsymbol{\sigma}_i\cdot\nabla\boldsymbol{u}\right\}+\int_{\Omega}\rho\boldsymbol{g}\cdot\boldsymbol{u}dx \\
&= -\int_{\Gamma_S}\beta_S|\mathbf{P}_S\boldsymbol{u}|^2ds-\gamma\int_{\Gamma(t)}\kappa V_\Gamma ds-\int_{\Omega}\frac{1}{2}|\mathbf{D}(\boldsymbol{u})|^2dx+\int_{\Omega}\rho\boldsymbol{g}\cdot\boldsymbol{u}dx. \qquad (2.17)
\end{aligned}
$$

where in the last equation, we have used the interface condition (2.2), the Navier slip boundary condition (2.3), the incompressibility condition in (2.1), and also the relation that $\mathbf{D}(\boldsymbol{u}):\nabla\boldsymbol{u}=\frac{1}{2}|\mathbf{D}(\boldsymbol{u})|^2$.

Add the two equations (2.16) and (2.17) together, we finish the proof of the proposition. ∎

For the model with contact angle hysteresis, we also have an energy dissipation relation, which characterizes the averaged behaviour of the system. In this case, we set

$$
\tilde{\mathcal{E}}_p=\int_{\Gamma_{S1}}\frac{1}{\epsilon}\int\gamma_{S1}(s,z)dzds+\int_{\Gamma_{S2}}\frac{1}{\epsilon}\int\gamma_{S2}(s,z)dzds+\int_{\Gamma}\gamma ds+\int_{\Omega}\rho\boldsymbol{g}\cdot\boldsymbol{x}dx, \qquad (2.18)
$$

Here $\frac{1}{\epsilon}\int\gamma_{Si}(s,z)dz$ denotes the averaged solid-liquid interface energy density in the normal direction of the contact line at a point s on S.

PROPOSITION 2.3. *Let* $(\boldsymbol{u},p)$ *be the solution of* (2.1)-(2.3) *coupled with the contact angle hysteresis model* (2.11)*, we have*

$$
\frac{d}{dt}(\tilde{\mathcal{E}}_p+\mathcal{E}_k)=-2\Phi.
$$

Proof. The proof of the proposition is similar to that of Proposition 2.2. The only difference is that the surface energy in ths solid surface is replaced by the averaged energy densities. This leads to the relation that

$$
\frac{d}{dt}\tilde{\mathcal{E}}_p = \int_{L(t)}\left(\cos\theta_a-\frac{1}{\epsilon}\int\cos\theta_Y(s,z)dz\right)u_Lds+\gamma\int_{\Gamma(t)}\kappa V_\Gamma ds-\int_{\Omega}\rho\boldsymbol{g}\cdot\boldsymbol{u}dx. \qquad (2.19)
$$

Then use the condition (2.11) and the same arguments as above lead to the conclusion of the proposition. ∎

The propositions 2.2 and 2.3 show that the macroscopic CAH model we considered is thermodynamically consistent. Furthermore, the interface energies in (2.18) have clear physical meaning for chemically inhomogeneous surfaces.

3. The variational formulae.

3.1. A standard weak formula. In the previous section, we rewrite several MCL models into a unified form. Now we derive a weak formula for the continuum equations. We first introduce some functional spaces,

$$
\begin{aligned}
\boldsymbol{X}_0 &:= \{\boldsymbol{v}\in(H^1(\Omega)^3):\boldsymbol{v}=\mathbf{0}\text{ on }\partial\Omega\setminus\Gamma_S,\boldsymbol{v}\cdot\boldsymbol{n}_S=0\text{ on }\Gamma_S\}, \\
Q &:= \left\{q\in L^2(\Omega):\int_{\Omega}qdx=0\right\}.
\end{aligned}
$$

For functions in $\boldsymbol{X}_0$ and Q, we define the following bilinear and trilinear forms, as well as some linear functionals,

$$
\begin{aligned}
m(\boldsymbol{u},\boldsymbol{v}) &:= \int_\Omega \rho \boldsymbol{u}\cdot \boldsymbol{v} dx,\\
a(\boldsymbol{u},\boldsymbol{v}) &:= \frac{1}{2}\int_\Omega \mu \mathbf{D}(\boldsymbol{u}):\mathbf{D}(\boldsymbol{v}) dx + \int_{\Gamma_S} \beta_S \mathbf{P}_S\boldsymbol{u}\cdot \mathbf{P}_S\boldsymbol{v} ds + \int_L \beta_L \boldsymbol{u}\cdot \boldsymbol{n}_L \boldsymbol{v}\cdot \boldsymbol{n}_L ds,\\
b(\boldsymbol{v},\boldsymbol{q}) &:= -\int_\Omega (\mathbf{div}\boldsymbol{v}) q dx, \quad c(\boldsymbol{w};\boldsymbol{u},\boldsymbol{v}) := \int_\Omega \rho(\boldsymbol{w}\cdot\nabla \boldsymbol{u})\cdot \boldsymbol{v} dx,\\
f_{\mathbf{ext}}(\boldsymbol{v}) &:= \int_\Omega \rho \boldsymbol{g}\cdot \boldsymbol{v} dx, \quad f_\Gamma(\boldsymbol{v}) := -\gamma \int_\Gamma \nabla_\Gamma \mathbf{id}_\Gamma : \nabla_\Gamma \boldsymbol{v} dx,\\
f_L(\boldsymbol{v}) &:= \gamma \int_L \psi(\theta_Y)\boldsymbol{v}\cdot \boldsymbol{n}_L ds.
\end{aligned}
$$

Here we set $\rho(x) = \begin{cases} \rho_1 & \text{if } x\in\Omega_1 \\ \rho_2 & \text{if } x\in \Omega_2 \end{cases}$, and $\mu(x) = \begin{cases} \mu_1 & \text{if } x\in\Omega_1 \\ \mu_2 & \text{if } x\in \Omega_2 \end{cases}$. Both of them are piecewisely constant functions. $\mathbf{id}_\Gamma(x) := x$, for $x \in \Gamma$ and ∇_Γ is the surface gradient operator on Γ [44]. In addition, we suppose that β_L and $\psi(\theta_Y)$ represent different parameter for different models(as shown in Table 1).

With the above notations, the weak formula for the two-phase Navier-Stokes equations (2.1)-(2.3) coupled with (2.12) can be written as follows. To find a pair $(\boldsymbol{u}, q) \in (\boldsymbol{X}_0, Q)$, such that

$$
m(\partial_t \boldsymbol{u},\boldsymbol{v}) + c(\boldsymbol{u};\boldsymbol{u},\boldsymbol{v}) + a(\boldsymbol{u},\boldsymbol{v}) + b(\boldsymbol{v},p) = f_{\mathbf{ext}}(\boldsymbol{v}) + f_\Gamma(\boldsymbol{v}) + f_L(\boldsymbol{v}), \forall \boldsymbol{v}\in \boldsymbol{X}_0; \tag{3.1}
$$

$$
b(\boldsymbol{u},q) = 0, \qquad \forall q \in Q. \tag{3.2}
$$

where the two-phase interface $\Gamma(t)$ moves with the normal velocity $V_\Gamma = \boldsymbol{u}\cdot\boldsymbol{n}_\Gamma$.

The derivation of the weak formula for Ren-E model can be found in [26]. For the other several models, the derivation is similar as the Ren-E model, since we have rewritten them into a similar form.

There exists several challenges to solve the weak problem numerically. The parameters in the system may have very large values. For example, the slip length parameter l_s is usually very small so that $\beta_S \gg 1$. Similarly, the parameter β_L may change from zero to infinity, especially for the model with contact angle hysteresis where $\beta_L = \xi_{hys}$ can be equal to $\xi_\infty \gg 1$. The very large parameters make direct discretization for (3.1)-(3.2) lead to algebraic systems with very large condition number.

3.2. A regularized weak formula. To avoid the numerical difficulties encountered in solving (3.1)-(3.2), we introduce a new regularized weak formula below. The main idea is to use a Nitsche type technique for general boundary conditions as in [41, 42]. The regularized weak form is the basis of our numerical method.

Let $h > 0$ be a given small parameter which is the mesh size in a numerical method. Let $u_n = \boldsymbol{u}\cdot\boldsymbol{n}_S$, $\boldsymbol{u}_\tau = \mathbf{P}_S\boldsymbol{u}$ on Γ_S and $u_L = \boldsymbol{u}\cdot\boldsymbol{n}_L$ on L where $\boldsymbol{n}_L$ is the out normal of L in the tangential surface of Γ_S. Similar notations are used also for a test function $\mathbf{v}$. We introduce some new notations,

$$
\begin{aligned}
a_h(\boldsymbol{u},\boldsymbol{v}) :=\ & \frac{1}{2}\int_\Omega \mu\mathbf{D}(\boldsymbol{u}) : \mathbf{D}(\boldsymbol{v})dx + \int_{\Gamma_S} \frac{\alpha_1\beta_S}{h\beta_S+\alpha_1}\boldsymbol{u}_\tau\cdot\boldsymbol{v}_\tau ds + \frac{\alpha_1}{h}\int_{\Gamma_S} u_n v_n ds \\
& - \int_{\Gamma_S} \frac{h\beta_S}{h\beta_S+\alpha_1} S(\boldsymbol{u},\boldsymbol{n})\cdot\boldsymbol{v}_\tau ds - \int_{\Gamma_S} \frac{h\beta_S}{h\beta_S+\alpha_1} S(\boldsymbol{v},\boldsymbol{n})\cdot\boldsymbol{u}_\tau ds \\
& - \int_{\Gamma_S} \frac{h}{h\beta_S+\alpha_1} S(\boldsymbol{u},\boldsymbol{n})\cdot S(\boldsymbol{v},\boldsymbol{n}) ds - \int_{\Gamma_S} \mu\boldsymbol{n}^T\mathbf{D}(\boldsymbol{u})\boldsymbol{n} v_n ds \\
& - \int_{\Gamma_S} \mu\boldsymbol{n}^T\mathbf{D}(\boldsymbol{v})\boldsymbol{n} u_n ds + \int_L \frac{\alpha_2\beta_L}{h\beta_L+\alpha_2} u_L v_L ds, \\
\tilde{b}(\boldsymbol{v},q) :=\ & \int_{\Gamma_S} q v_n ds - \int_\Omega (\mathbf{div}\boldsymbol{v}) q dx, \\
\tilde{c}(\boldsymbol{u};\boldsymbol{u},\boldsymbol{v}) :=\ & \frac{1}{2}c(\boldsymbol{u};\boldsymbol{u},\boldsymbol{v}) - \frac{1}{2}c(\boldsymbol{u};\boldsymbol{v},\boldsymbol{u}) \\
f_{L,h}(\boldsymbol{v}) :=\ & \gamma\int_L \psi(\theta_Y) v_L ds + \gamma\int_L v_n \sin\theta_a ds - \gamma\int_L \frac{h\beta_L}{h\beta_L+\alpha_2}(\psi(\theta_Y)-\cos\theta_a) v_L ds,
\end{aligned}
$$

where $\alpha_i, i=1,2$ are positive parameters of order $O(1)$. We can easily see that the coefficients satisfy $\lim_{\beta_S\to\infty}\frac{\alpha_1\beta_S}{h\beta_S+\alpha_1} = \frac{\alpha_1}{h}$, $\lim_{\beta_S\to\infty}\frac{h\beta_S}{h\beta_S+\alpha_1} = 1$, $\lim_{\beta_L\to\infty}\frac{\alpha_2\beta_L}{h\beta_L+\alpha_2} = \frac{\alpha_2}{h}$, etc. This implies that all the coefficients in the above definitions are uniformly bounded even when β_S and β_L go to infinity.

We then introduce a functional space

$$\boldsymbol{X} := \{\boldsymbol{v}\in(H^1(\Omega)^3) : \boldsymbol{v}=\mathbf{0} \text{ on } \partial\Omega\setminus\Gamma_S\}.$$

The regularized problem is defined as follows. To find a pair $(\boldsymbol{u},q)\in(\boldsymbol{X},Q)$, such that

$$m(\partial_t\boldsymbol{u},\boldsymbol{v}) + \tilde{c}(\boldsymbol{u};\boldsymbol{u},\boldsymbol{v}) + a_h(\boldsymbol{u},\boldsymbol{v}) + \tilde{b}(\boldsymbol{v},p) = f_{\mathbf{ext}}(\boldsymbol{v}) + f_\Gamma(\boldsymbol{v}) + f_{L,h}(\boldsymbol{v}), \forall\boldsymbol{v}\in\boldsymbol{X}; \tag{3.3}$$

$$\tilde{b}(\boldsymbol{u},q) = 0, \qquad \forall q\in Q. \tag{3.4}$$

where the two-phase interface $\Gamma(t)$ moves with the normal velocity $V_\Gamma = \boldsymbol{u}\cdot\boldsymbol{n}_\Gamma$. In the weak formula, all the boundary conditions on Γ_S are imposed weakly by a Nitcshe type technique. In addition, we use an antisymmetric representation $\tilde{c}$ for the convection term.

3.3. Consistency. The following theorem show the consistency of the regularized weak formula (3.3)-(3.4) with two-phase Navier-Stokes equations described in Section 2.

THEOREM 3.1. *If* $(\boldsymbol{u},p)$ *is a solution of the equations* (2.1)-(2.3) *coupled with the boundary condition* (2.12)*, then the pair* $(\boldsymbol{u},p)$ *also satisfies the weak problem* (3.3)-(3.4).

Proof. It is easy to see that the equation (3.4) can be simply obtained by the second equation of (2.1) and the fact that $u_n = 0$ on Γ_S.

We now prove the equation (3.3). We multiply the first equation in (2.1) by a function $\boldsymbol{v}\in\boldsymbol{X}$ and integrate in Ω_i respectively. We have

$$\int_{\Omega_i}\rho_i\left(\frac{\partial\boldsymbol{u}}{\partial t} + \boldsymbol{u}\cdot\nabla\boldsymbol{u}\right)\cdot\boldsymbol{v}dx = \int_{\Omega_i}(\mathbf{div}\boldsymbol{\sigma}_i + \rho_i\boldsymbol{g})\cdot\boldsymbol{v}dx. \tag{3.5}$$

By adding the equations together for $i = 1, 2$, the left hand side terms lead to $m(\partial_t \boldsymbol{u}, \boldsymbol{v}) + \tilde{c}(\boldsymbol{u}; \boldsymbol{u}, \boldsymbol{v})$. Here we have used the fact that

$$\sum_{i=1}^{2} \int_{\Omega_i} \frac{1}{2} \mathbf{u} \cdot \nabla \mathbf{u} \cdot \mathbf{v} dx = -\sum_{i=1}^{2} \int_{\Omega_i} \frac{1}{2} \mathbf{u} \cdot \nabla \mathbf{v} \cdot \mathbf{u} dx,$$

which is obtained by integration by part and the conditions $\nabla \cdot \mathbf{u} = 0$ in Ω_i, $\mathbf{u} \cdot \mathbf{n} = 0$ on $\partial\Omega$ and $[\mathbf{u}] = 0$ on Γ. In addition, it is easy to see that the second term in the right hand side of (3.5) gives $f_{\mathbf{ext}}(\boldsymbol{v})$. We need only to consider the first term in right hand side of the equation (3.5). Direct calculations give

$$\begin{aligned}
\int_{\Omega_i} \mathbf{div} \boldsymbol{\sigma}_i \cdot \boldsymbol{v} dx &= \int_{\partial\Omega_i} (\boldsymbol{\sigma}_i \boldsymbol{n}) \cdot \boldsymbol{v} ds - \int_{\Omega_i} \boldsymbol{\sigma}_i : \nabla \boldsymbol{v} dx \\
&= \int_{\partial\Omega_i} (\boldsymbol{\sigma}_i \boldsymbol{n}) \cdot \boldsymbol{v} ds + \int_{\Omega_i} p(\nabla \cdot \boldsymbol{v}) dx - \frac{\mu_i}{2} \int_{\Omega_i} \mathbf{D}(\boldsymbol{u}) : \mathbf{D}(\boldsymbol{v}) dx.
\end{aligned}$$

Summarize the equation for $i = 1, 2$, we have

$$\begin{aligned}
&\sum_{i=1}^{2} \int_{\Omega_i} \mathbf{div} \boldsymbol{\sigma}_i \cdot \boldsymbol{v} dx \\
&= \int_{\Gamma_S} (\boldsymbol{\sigma} \boldsymbol{n}_{\boldsymbol{S}}) \cdot \boldsymbol{v} ds + \int_{\Gamma} [\boldsymbol{\sigma}_i \boldsymbol{n}_{\boldsymbol{\Gamma}}] \cdot \boldsymbol{v} ds + \int_{\Omega} p(\nabla \cdot \boldsymbol{v}) dx - \int_{\Omega} \frac{\mu}{2} \mathbf{D}(\boldsymbol{u}) : \mathbf{D}(\boldsymbol{v}) dx \\
&= \int_{\Gamma_S} \mathbf{P}_S \boldsymbol{\sigma} \boldsymbol{n}_S \cdot \boldsymbol{v}_\tau ds + \int_{\Gamma_S} \boldsymbol{n}_S^T \boldsymbol{\sigma} \boldsymbol{n}_S v_n ds - \gamma \int_{\Gamma} \kappa \boldsymbol{n}_\Gamma \cdot \boldsymbol{v} ds \\
&\quad + \int_{\Omega} p(\nabla \cdot \boldsymbol{v}) dx - \int_{\Omega} \frac{\mu}{2} \mathbf{D}(\boldsymbol{u}) : \mathbf{D}(\boldsymbol{v}) dx. \qquad (3.6)
\end{aligned}$$

By using the Navier slip boundary condition (2.3), we have

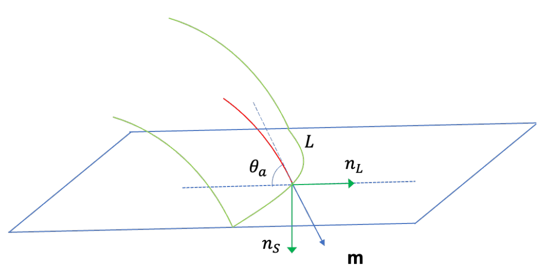

Figure 1: Vectors near the contact line.

$$\int_{\Gamma_S} \mathbf{P}_S \boldsymbol{\sigma} \boldsymbol{n}_S \cdot \boldsymbol{v}_\tau ds = -\int_{\Gamma_S} \beta_S \boldsymbol{u}_\tau \cdot \boldsymbol{v}_\tau ds.$$

We can also compute

$$\int_{\Gamma_S} \boldsymbol{n}_S^T \boldsymbol{\sigma} \boldsymbol{n}_S v_n ds = -\int_{\Gamma_S} p v_n ds + \int_{\Gamma_S} \mu \boldsymbol{n}_S^T \mathbf{D}(\boldsymbol{v}) \boldsymbol{n}_S v_n ds.$$

Notice the fact that $-\Delta_\Gamma \mathbf{id}_\Gamma(x) = \kappa(x)\boldsymbol{n}_\Gamma$ where Δ_Γ is the Laplace-Beltrami operator (c.f. [44]). By integration by part, the third term in the right hand side of (3.6) leads to

$$
\begin{aligned}
-\gamma \int_\Gamma \kappa \boldsymbol{n}_\Gamma \cdot \boldsymbol{v} ds &= \gamma \int_L \boldsymbol{m}^T (\nabla_\Gamma \mathbf{id}_\Gamma)\boldsymbol{v} ds - \gamma \int_{\Gamma_S} \nabla_\Gamma \mathbf{id}_\Gamma \cdot \nabla_\Gamma \boldsymbol{v} ds \\
&= \gamma \int_L \boldsymbol{m}^T \mathbf{P}_\Gamma \boldsymbol{v} ds - \gamma \int_{\Gamma_S} \nabla_\Gamma \mathbf{id}_\Gamma \cdot \nabla_\Gamma \boldsymbol{v} ds \\
&= \gamma \int_L v_L \cos\theta_a + v_n \sin\theta_a ds - \gamma \int_{\Gamma_S} \nabla_\Gamma \mathbf{id}_\Gamma \cdot \nabla_\Gamma \boldsymbol{v} ds \\
&= -\int_L \beta_L u_L v_L ds + \gamma \int_L v_L \psi(\theta_Y) + v_n \sin\theta_a ds - \gamma \int_{\Gamma_S} \nabla_\Gamma \mathbf{id}_\Gamma \cdot \nabla_\Gamma \boldsymbol{v} ds \\
&= -\int_L \beta_L u_L v_L ds + \gamma \int_L v_L \psi(\theta_Y) + v_n \sin\theta_a ds + f_\Gamma(\boldsymbol{v}).
\end{aligned}
$$

Here $\boldsymbol{m}$ is out normal of L in the tangential surface of Γ, the relation $\boldsymbol{m}^T \mathbf{P}_\Gamma \boldsymbol{v} = \mathbf{v} \cdot \mathbf{m} = v_L \cos\theta_a + v_n \sin\theta_a$ can be seen from Figure 1, and we also have used the boundary condition (2.12) for MCLs. Combining the above calculations, we are led to

(3.7)
$$
\begin{aligned}
&m(\partial_t \boldsymbol{u}, \boldsymbol{v}) + \tilde{c}(\boldsymbol{u}; \boldsymbol{u}, \boldsymbol{v}) + \int_\Omega \frac{\mu}{2} \mathbf{D}(\boldsymbol{u}) : \mathbf{D}(\boldsymbol{v}) dx + \int_{\Gamma_S} \beta_S \boldsymbol{u}_\tau \cdot \boldsymbol{v}_\tau ds + \int_L \beta_L u_L v_L ds \\
&- \int_{\Gamma_S} \mu \boldsymbol{n}_S^T \mathbf{D}(\boldsymbol{v}) \boldsymbol{n}_S v_n ds + \tilde{b}(\boldsymbol{v}, p) = f_{\mathbf{ext}}(\boldsymbol{v}) + \gamma \int_L \boldsymbol{v} \cdot \boldsymbol{n}_L \psi(\theta_Y) + v_n \sin\theta_a ds + f_\Gamma(\boldsymbol{v}).
\end{aligned}
$$

Noticing the Navier slip boundary condition (2.3) on Γ_S, the boundary condition (2.12) on L, and also the definition of $S(\boldsymbol{u}, \boldsymbol{n}) = \mu \mathbf{P}_S \mathbf{D}(\boldsymbol{u}) \boldsymbol{n}_S = \mathbf{P}_S \boldsymbol{\sigma} \boldsymbol{n}_S$, we can further derive the relation that

$$
\begin{aligned}
a_h(\boldsymbol{u}, \boldsymbol{v}) = &\frac{1}{2} \int_\Omega \mu \mathbf{D}(\boldsymbol{u}) : \mathbf{D}(\boldsymbol{v}) dx + \int_{\Gamma_S} \frac{\alpha_1 \beta_S}{h\beta_S + \alpha_1} \boldsymbol{u}_\tau \cdot \boldsymbol{v}_\tau ds \\
&- \int_{\Gamma_S} \frac{h\beta_S}{h\beta_S + \alpha_1} \mathbf{P}_S \boldsymbol{\sigma} \boldsymbol{n}_S \cdot \boldsymbol{v}_\tau ds - \int_{\Gamma_S} \frac{h\beta_S}{h\beta_S + \alpha_1} S(\boldsymbol{v}, \boldsymbol{n}) \cdot \boldsymbol{u}_\tau ds \\
&- \int_{\Gamma_S} \frac{h}{h\beta_S + \alpha_1} \mathbf{P}_S \boldsymbol{\sigma} \boldsymbol{n}_S \cdot S(\boldsymbol{v}, \boldsymbol{n}) ds - \int_{\Gamma_S} \mu \boldsymbol{n}^T \mathbf{D}(\boldsymbol{u}) \boldsymbol{n} v_n ds \\
&+ \int_L \frac{\alpha_2 \beta_L}{h\beta_L + \alpha_3} u_L v_L ds \\
= &\frac{1}{2} \int_\Omega \mu \mathbf{D}(\boldsymbol{u}) : \mathbf{D}(\boldsymbol{v}) dx + \int_{\Gamma_S} \frac{\alpha_1 \beta_S}{h\beta_S + \alpha_1} \boldsymbol{u}_\tau \cdot \boldsymbol{v}_\tau ds \\
&+ \int_{\Gamma_S} \frac{h\beta_S}{h\beta_S + \alpha_1} \beta_S \boldsymbol{u}_\tau \cdot \boldsymbol{v}_\tau ds - \int_{\Gamma_S} \mu \boldsymbol{n}^T \mathbf{D}(\boldsymbol{u}) \boldsymbol{n} v_n ds + \int_L \frac{\alpha_2 \beta_L}{h\beta_L + \alpha_3} u_L v_L ds \\
= &\frac{1}{2} \int_\Omega \mu \mathbf{D}(\boldsymbol{u}) : \mathbf{D}(\boldsymbol{v}) dx + \int_{\Gamma_S} \beta_S \boldsymbol{u}_\tau \cdot \boldsymbol{v}_\tau ds - \int_{\Gamma_S} \mu \boldsymbol{n}^T \mathbf{D}(\boldsymbol{u}) \boldsymbol{n} v_n ds \\
&+ \int_L \beta_L \left(1 - \frac{h\beta_L}{h\beta_L + \alpha_2}\right) u_L v_L ds
\end{aligned}
$$

$$= \frac{1}{2}\int_\Omega \mu \mathbf{D}(\boldsymbol{u}) : \mathbf{D}(\boldsymbol{v}) dx + \int_{\Gamma_S} \beta_S \boldsymbol{u}_\tau \cdot \boldsymbol{v}_\tau ds - \int_{\Gamma_S} \mu \boldsymbol{n}^T \mathbf{D}(\boldsymbol{u})\boldsymbol{n} v_n ds + \int_L \beta_L u_L v_L ds$$
$$-\gamma \int_L \frac{h\beta_L}{h\beta_L + \alpha_2}(\psi(\theta_Y) - \cos\theta_a) v_L ds.$$

Submit the equation into (3.7) and notice the definition of $f_{L,h}$, we obtain (3.3). ◻

Based on the weak formula (3.3)-(3.4), we develop a stable finite element method for the two-phase flow with MCLs as shown in the following sections.

4. The discrete problem.

Before we introduce the discrete problem, we first introduce the level-set method to capture the motion of the two-phase interface. Let $\phi(x,t)$ be a smooth level-set function corresponding to $\Gamma(t)$, namely

$$\Gamma(t) = \{x \in \Omega | \phi(x,t) = 0\}.$$

Then the motion of $\Gamma(t)$ can be described by the equation

$$\frac{\partial \phi}{\partial t} + \boldsymbol{u} \cdot \nabla \phi = 0. \tag{4.1}$$

The equation will be solved together with the system (3.3)-(3.4).

4.1. The finite element discretization.

Let $\mathcal{T}_h$ be a regular triangulation of Ω with mesh size h. We define some finite element spaces as follows. To discretize the level-set function, we use the standard P_2-FEM approach and denoted by

$$V_h := \{\phi_h \in C(\Omega) : \phi_h|_T \in \mathcal{P}_2, \forall T \in \mathcal{T}_h\}.$$

To discretize the velocity, we choose the P_2 finite element vector space and define

$$\boldsymbol{X}_h := \{\boldsymbol{v}_h \in C(\Omega) : \boldsymbol{v}_h|_T \in (\mathcal{P}_2)^3 \text{ for all } T \in \mathcal{T}_h, \boldsymbol{v_h}|_{\partial\Omega\setminus\Gamma_S} = 0\}.$$

For the pressure, we use an extended finite element method(XFEM) defined as follows. Let the discrete interface Γ_h generated by the discrete level-set function ϕ_h [44]. The domain Ω is divided by Γ_h into two parts $\Omega_{i,h}$, $i = 1, 2$. We introduce two subdomains $\Omega^o_{i,h}$ that overlap across the discrete interface as,

$$\Omega^o_{i,h} := \cup_{T\in\mathcal{T}_h, \text{meas}_3(T\cap\Omega_{i,h})>0} T.$$

The corresponding P_1 finite element spaces are defined as

$$Q_{i,h} := \{q \in C(\Omega^o_{i,h}) | q_h|_T \in \mathcal{P}_1 \text{ for all } T \in \Omega^o_{i,h}\}.$$

Then for a pair $p_h = (p_{1,h}, p_{2,h}) \in Q_{1,h} \times Q_{2,h}$, it may have two values in the overlapped region. We define a uni-valued function p_h^Γ as

$$p_h^\Gamma(x) = p_{i,h}(x), \quad \text{for } x \in \Omega_{i,h}.$$

Notice that the function in p_h^Γ may be discontinuous across Γ_h and we can use it to approximate pressure. The XFEM space is defined as

$$Q_h^\Gamma := \{p_h \in Q_{1,h} \times Q_{2,h} | \int_\Omega p_h^\Gamma(x) dx = 0.\}.$$

It is known that the resulted algebraic system may be ill-conditioned if one element T is cut by Γ_h into two subsets with very large volume ratio(i.e. the volume of one subset is close to zero). To avoid the difficulty, many different techniques can be applied [45, 26]. Typically one can either simply remove the basis functions with small support in the finite element space Q_h^Γ [46] or add some ghost penalty terms to the weak form [45, 26]. In our numerical experiments, we stabilize the problem using the ghost penalty techniques. That is to add some penalty terms in the bilinear form, i.e.

$$j(p_h, q_h) := \sum_{i=1}^{2} j_i(p_{i,h}, q_{i,h}), \qquad p_h, q_h \in Q_{1,h} \times Q_{2,h}$$

$$\text{with} \qquad j_i(p_{i,h}, q_{i,h}) := \mu_i^{-1} \sum_{F \in \mathcal{F}_i} h_F^3([\nabla p_{i,h} \cdot n_F], [\nabla q_{i,h} \cdot n_F])_{0,F.}$$

where h_F is the diameter of the face F and $[\nabla p_{i,h} \cdot n_F]$ denotes the jump of the normal components of the piecewise constant function $\nabla p_{i,h}$ across the face F. Here $\mathcal{F}_i$ is the set of surfaces of elements that intersect with Γ_h minus the boundary of $\Omega_{i,h}^o$. More details on the definition of the XFEM and the stabilization terms can be found for example in [26].

With the above notations, we can introduce the semi-discrete problem as follows. To find a pair of functions $(\boldsymbol{u}_h, p_h)$ and a function ϕ_h satisfying,

(4.2)

$$\begin{aligned} m(\partial_t \boldsymbol{u}_h, \boldsymbol{v}_h) + \tilde{c}(\boldsymbol{u}_h; \boldsymbol{u}_h, \boldsymbol{v}_h) + a_h(\boldsymbol{u}_h, \boldsymbol{v}_h) + \tilde{b}(\boldsymbol{v}_h, p_h) - \tilde{b}(\boldsymbol{u}_h, q_h) + \alpha_3 j(p_h, q_h) \\ = f_{\mathbf{ext}}(\boldsymbol{v}_h) + f_\Gamma(\boldsymbol{v}_h) + f_{L,h}(\boldsymbol{v}_h), \qquad \forall \boldsymbol{v}_h \in \boldsymbol{X}_h, q_h \in Q_h^\Gamma; \end{aligned}$$

$$(\partial_t \phi_h + \boldsymbol{u}_h \cdot \nabla \phi_h, \varphi_h + \delta_T \boldsymbol{u}_h \cdot \nabla \varphi_h) = 0, \qquad \forall \varphi_h \in V_h. \tag{4.3}$$

Here $(\cdot, \cdot)$ represents the L^2 inner product on Ω. In the above equations, all the integrals on $\Gamma(t)$ and $L(t)$ will be replaced by those on the discrete interface $\Gamma_h(t)$ and the discrete contact line $L_h(t) := \bar{\Gamma}_h \cap \Gamma_S$. In addition, we use the the streamline diffusion finite element (SDFEM) to stabilize the discretization of the convection equation for the levelset function and $\delta_T = c \frac{h_T}{\max(\varepsilon_0, \|\boldsymbol{u}_h\|_{\infty,T})}$ with $\varepsilon_0 > 0$ and $c = O(1)$ is a stabilization parameter.

4.2. The fully discrete scheme. The fully discrete scheme is simply to replace the time derivative in (4.2)-(4.3) by a finite difference scheme. Let $0 = t_0 < t_1 < \cdots < t_N = T$ be a partition of a time interval $(0, T)$. Denote by $(\boldsymbol{u}_h^k, p_h^k, \phi_h^k)$ the discrete solution on the time t_k and let $\Delta t_k = t_k - t_{k-1}$. Then the fully implicit backward Euler scheme can be defined as

$$\begin{aligned} m\left(\phi_h^k; \frac{\boldsymbol{u}_h^k - \boldsymbol{u}_h^{k-1}}{\Delta t_k}, \boldsymbol{v}_h\right) + \tilde{c}(\phi_h^k; \boldsymbol{u}_h^k; \boldsymbol{u}_h^k, \boldsymbol{v}_h) + a_h(\phi_h^k; \boldsymbol{u}_h^k, \boldsymbol{v}_h) + \tilde{b}(\phi_h^k; \boldsymbol{v}_h, p_h^k) \\ - \tilde{b}(\phi_h^k; \boldsymbol{u}_h^k, q_h) + j(\phi_h^k; p_h, q_h) = f_{\mathbf{ext}}(\phi_h^k; \boldsymbol{v}_h) + f_\Gamma(\phi_h^k; \boldsymbol{v}_h) + f_{L,h}(\phi_h^k; \boldsymbol{v}_h), \\ \forall \boldsymbol{v}_h \in \boldsymbol{X}_h, q_h \in Q_h^\Gamma(\phi_h^k); \end{aligned} \tag{4.4}$$

$$\left(\frac{\phi_h^k - \phi_h^{k-1}}{\Delta t_k} + \boldsymbol{u}_h^k \cdot \nabla \phi_h^k, \varphi_h + \delta_T \boldsymbol{u}_h^k \cdot \nabla \varphi_h\right) = 0. \qquad \forall \varphi_h \in V_h. \tag{4.5}$$

Notice all the linear, bilinear, and trilinear forms in the above equations are written in a way to explicitly show their dependence on ϕ_h^k. Notice that all the integration in these terms depends on the location of the discrete interface and the discrete contact line, which is described by ϕ_h^k. For example, we have

$$m(\phi_h^k; \boldsymbol{v}_h, \boldsymbol{v}_h) = \sum_{i=1}^{2} \int_{\Omega_{i,h}^k} \boldsymbol{v}_h \cdot \boldsymbol{v}_h dx,$$

where $\Omega_{i,h}^k$ are the subsets of Ω separated by $\Gamma_h^k := \{x \in \Omega : \phi_h^k(x) = 0\}$.

There are several issues to solve the fully discrete problem. Firstly, the equation is a fully coupled nonlinear equation. We can solve it by iterative methods. Secondly, the reparametrization of the level-set function is needed to keep the gradient $|\nabla\phi_h|$ away from zero. Thirdly, we may need to adjust ϕ_h every a few time steps to keep the volume in Ω_i conserved. All these issues have been discussed extensively in literature, c.f. [26, 44].

In applications, it is more convenient to solve a decoupled problem which is described as follows. For given solution $(\boldsymbol{u}_h^{k-1}, p_h^{k-1}, \phi_h^{k-1})$ in the $(k-1)$-th step, we first solve

(4.6)

$$m\Big(\phi_h^{k-1}; \frac{\boldsymbol{u}_h^k - \boldsymbol{u}_h^{k-1}}{\Delta t_k}, \boldsymbol{v}_h\Big) + \tilde{c}(\phi_h^{k-1}; \boldsymbol{u}_h^{k-1}; \boldsymbol{u}_h^k, \boldsymbol{v}_h) + a_h(\phi_h^{k-1}; \boldsymbol{u}_h^k, \boldsymbol{v}_h) + \tilde{b}(\phi_h^{k-1}; \boldsymbol{v}_h, p_h^k)$$

$$- \tilde{b}(\phi_h^{k-1}; \boldsymbol{u}_h^k, q_h) + j(\phi_h^{k-1}; p_h, q_h) = f_{\mathbf{ext}}(\phi_h^{k-1}; \boldsymbol{v}_h) + f_\Gamma(\phi_h^{k-1}; \boldsymbol{v}_h) + f_{L,h}(\phi_h^{k-1}; \boldsymbol{v}_h),$$

$$\forall \boldsymbol{v}_h \in \boldsymbol{X}_h, q_h \in Q_h^\Gamma(\phi_h^{k-1});$$

to get a solution $(\boldsymbol{u}_h^k, p_h^k)$. Then we solve

$$\left(\frac{\phi_h^k - \phi_h^{k-1}}{\Delta t_k} + \boldsymbol{u}_h^k \cdot \nabla\phi_h^k, \varphi_h + \delta_T \boldsymbol{u}_h^k \cdot \nabla\varphi_h\right) = 0, \qquad \forall \varphi_h \in V_h, \tag{4.7}$$

to obtain ϕ_h^k. When the time step is small and the interface does not change much in one time step, the decoupled scheme is a good approximation to the coupled problem (4.4)-(4.5).

5. Well-posedness of the fully discrete problem. In this section, we prove the well-posedness of the decoupled scheme (4.6)-(4.7). For simplicity in notations, we ignore the explicit dependence on ϕ_h^{k-1} in the formulae. All the integrals are done on Γ_h^{k-1} or in the domains separated by the interface. The constants in the following estimates is independent of the mesh size h, the large friction coefficient β_S and β_L, and also independent of how the triangulation intersects with the interface. This implies the stability of the discrete problem..

We first introduce some discrete norms. For the discrete velocity, we define

$$\|\boldsymbol{u}_h\|_h^2 := \int_\Omega \alpha_0 |\boldsymbol{u}_h|^2 dx + \frac{1}{4}\int_\Omega \mu |\mathbf{D}(\boldsymbol{u}_h)|^2 dx + \int_{\Gamma_S} \frac{\alpha_1\beta_S}{2(h\beta_S + \alpha_1)} |\boldsymbol{u}_{h,\tau}|^2 ds$$

$$+ \frac{\alpha_1}{2h}\int_{\Gamma_S} |u_{h,n}|^2 ds + \int_L \frac{\alpha_2\beta_L}{h\beta_L + \alpha_2} |u_{h,L}|^2 ds,$$

where $\alpha_0 = \frac{\rho}{\Delta t}$. Then we define a norm for the pair $(\boldsymbol{u}_h, p_h) \in \boldsymbol{X}_h \times Q_h^\Gamma$,

$$|||(\boldsymbol{u}_h, p_h)|||_h^2 := \|\boldsymbol{u}_h\|_h^2 + \left\|\mu^{-\frac{1}{2}} p_h\right\|_{0,\Omega_{1,h}\cup\Omega_{2,h}}^2 + j(p_h, p_h).$$

The following lemma show the inf-sup condition for $\tilde{b}(\cdot,\cdot)$.

LEMMA 5.1. *Let Γ_h^{k-1} be a non-degenerate interface. Then there exists a $h_0 > 0$ and $c_1, c_2 > 0$ such that for all $h \le h_0$,*

$$\sup_{\boldsymbol{v}_h \in \boldsymbol{X}_h} \frac{\tilde{b}(\boldsymbol{v}_h, q_h)}{\|\boldsymbol{v}_h\|_h} \ge c_1 \|\mu^{-\frac{1}{2}} q_h\|_{0,\Omega_{1,h}\cup\Omega_{2,h}} - c_2 \frac{j(q_h, q_h)}{\|\mu^{-\frac{1}{2}} q_h\|_{0,\Omega_{1,h}\cup\Omega_{2,h}}}, \qquad \forall q_h \in Q_h^\Gamma.$$

Proof. The result is a direct generation of a result in [47]. There it is proved that for any $q_h \in Q_h^\Gamma$, there exists a function $\boldsymbol{v}_h \in \boldsymbol{X}_{h,0}$ ($\boldsymbol{v}_h = 0$ on $\partial\Omega$), such that

$$\frac{\int_\Omega (\mathbf{div}\boldsymbol{v}_h) q_h dx}{\|\mu^{\frac{1}{2}} \nabla \boldsymbol{v}_h\|_0} \ge c_1 \|\mu^{-\frac{1}{2}} q_h\|_{0,\Omega_{1,h}\cup\Omega_{2,h}} - c_2 \frac{j(q_h, q_h)}{\|\mu^{-\frac{1}{2}} q_h\|_{0,\Omega_{1,h}\cup\Omega_{2,h}}}.$$

Notice that for $\boldsymbol{v}_h \in \boldsymbol{X}_{h,0} \subset \boldsymbol{X}_h$, we have

$$\tilde{b}(\boldsymbol{v}_h, q_h) = \int_\Omega (\mathbf{div}\boldsymbol{v}_h) q_h dx + \int_{\Gamma_S} v_n q_h dx = \int_\Omega (\mathbf{div}\boldsymbol{v}_h) q_h dx,$$

and also $\|\boldsymbol{v}_h\|_h = \left(\frac{1}{4}\int_\Omega \mu |\mathbf{D}(\boldsymbol{v}_h)|^2 dx + \int_\Omega \alpha_0 |\boldsymbol{u}_h|^2 dx\right)^{\frac{1}{2}} \le c\|\mu^{\frac{1}{2}} \nabla \boldsymbol{v}_h\|_0$. Here we use the Kohn inequality. Then we have

$$\frac{\tilde{b}_h(\boldsymbol{v}_h, q_h)}{\|\boldsymbol{v}_h\|_h} \ge \frac{\int_\Omega (\mathbf{div}\boldsymbol{v}_h) q_h dx}{c\|\mu^{\frac{1}{2}} \nabla \boldsymbol{v}_h\|_0} \ge \frac{c_1}{c} \|\mu^{-\frac{1}{2}} q_h\|_{0,\Omega_{1,h}\cup\Omega_{2,h}} - \frac{c_2}{c} \frac{j(q_h, q_h)}{\|\mu^{-\frac{1}{2}} q_h\|_{0,\Omega_{1,h}\cup\Omega_{2,h}}}.$$

This concludes the proof of the lemma. ∎

The following lemma is on the continuity of a_h. The proof is trivial and we simply ignore it.

LEMMA 5.2. *There exists a constant $c_3 > 0$, such that*

$$m(\alpha_0 \boldsymbol{u}_h, \boldsymbol{v}_h) + \tilde{c}(\boldsymbol{u}_h^{n-1}; \boldsymbol{u}_h, \boldsymbol{v}_h) + a_h(\boldsymbol{u}_h, \boldsymbol{v}_h) \le c_3 \|\boldsymbol{u}_h\|_h \|\boldsymbol{v}_h\|_h.$$

The next lemma states the coercivity of the bilinear forms.

LEMMA 5.3. *Let Γ_h^{k-1} is a non-degenerate interface. Then for given $h_0 > 0$, there exists a constant $c_4 > 0$ such that*

$$m(\alpha_0 \boldsymbol{u}_h, \boldsymbol{u}_h) + b_h(\boldsymbol{u}_h^{n-1}; \boldsymbol{u}_h, \boldsymbol{u}_h) + a_h(\boldsymbol{u}_h, \boldsymbol{u}_h) \ge \|\boldsymbol{u}_h\|_h^2$$

for all $h \le h_0$ and $\alpha_1 \ge c_4$.

Proof. By definition, $b_h(\boldsymbol{u}_h^{n-1}; \boldsymbol{u}_h, \boldsymbol{u}_h) = 0$. Direct calculations show that

$$\begin{aligned}
a_h(\boldsymbol{u}_h, \boldsymbol{u}_h) = &\frac{1}{2}\int_\Omega \mu |\mathbf{D}(\boldsymbol{u_h})|^2 dx + \int_{\Gamma_S} \frac{\alpha_1 \beta_S}{h\beta_S + \alpha_1} |\boldsymbol{u}_{h,\tau}|^2 ds + \frac{\alpha_1}{h}\int_{\Gamma_S} |u_{h,n}|^2 ds \\
&- \int_{\Gamma_S} \frac{2h\beta_S}{h\beta_S + \alpha_1} \mu \mathbf{P}_S \mathbf{D}(\boldsymbol{u}_h)\boldsymbol{n}_S \cdot \boldsymbol{u}_{h,\tau} ds - \int_{\Gamma_S} \frac{h}{h\beta_S + \alpha_1} |\mu \mathbf{P}_S \mathbf{D}(\boldsymbol{u}_h)\boldsymbol{n}_S|^2 ds \\
&- 2\int_{\Gamma_S} \mu \boldsymbol{n}^T \mathbf{D}(\boldsymbol{u_h})\boldsymbol{n} u_n ds + \int_L \frac{\alpha_2 \beta_L}{h\beta_L + \alpha_2} |u_{h,L}|^2 ds.
\end{aligned}$$

Notice that

$$\begin{aligned}
\int_{\Gamma_S} \frac{2h\beta_S}{h\beta_S + \alpha_1} \mu \mathbf{P}_S \mathbf{D}(\boldsymbol{u}_h)\boldsymbol{n}_S \cdot \boldsymbol{u}_{h,\tau} ds \le &\frac{1}{2}\int_{\Gamma_S} \frac{\alpha_1 \beta_S}{h\beta_S + \alpha_1} |\boldsymbol{u}_{h,\tau}|^2 ds \\
&+ 2\int_{\Gamma_S} \frac{h^2 \beta_S}{(h\beta_S + \alpha_1)\alpha_1} |\mu \mathbf{P}_S \mathbf{D}(\boldsymbol{u}_h)\boldsymbol{n}_S|^2 ds,
\end{aligned}$$

and

$$2\int_{\Gamma_S}\mu\boldsymbol{n}^T\mathbf{D}(\boldsymbol{u_h})\boldsymbol{n}u_n ds \le \frac{\alpha_1}{2h}\int_{\Gamma_S}|u_{h,n}|^2 ds + \frac{2h}{\alpha_1}\int_{\Gamma_S}|\mu\boldsymbol{n}^T\mathbf{D}(\boldsymbol{u_h})\boldsymbol{n}|^2 ds.$$

Then we have

$$\begin{aligned} a_h(\boldsymbol{u}_h,\boldsymbol{u}_h) \ge& \left(\frac{1}{2} - \frac{2h^2\beta_S\mu}{(h\beta_S+\alpha_1)\alpha_1} - \frac{h\mu}{h\beta_S+\alpha_1} - \frac{2h\mu}{\alpha_1}\right)\int_\Omega \mu|\mathbf{D}(\boldsymbol{u_h})|^2 dx \\ &+ \int_{\Gamma_S}\frac{\alpha_1\beta_S}{2(h\beta_S+\alpha_1)}|\boldsymbol{u}_{h,\tau}|^2 ds + \frac{\alpha_1}{2h}\int_{\Gamma_S}|u_{h,n}|^2 ds + \int_L \frac{\alpha_2\beta_L}{h\beta_L+\alpha_2}|u_{h,L}|^2 ds. \end{aligned}$$

For any $h \le h_0$, there exists a $c_4 > 0$ such that for any $\alpha_1 > c_4$, we have $\frac{1}{2} - \frac{2h^2\beta_S\mu}{(h\beta_S+\alpha_1)\alpha_1} - \frac{h\mu}{h\beta_S+\alpha_1} - \frac{2h\mu}{\alpha_1} \ge \frac{1}{4}$. Then the above inequality implies the conclusion of the Lemma. ∎

Denote by

$$\begin{aligned} A((\boldsymbol{u}_h,p_h),(\boldsymbol{v}_h,q_h)) :=& m(\alpha_0\boldsymbol{u}_h,\boldsymbol{v}_h) + c_h(\boldsymbol{u}_h^{n-1};\boldsymbol{u}_h,\boldsymbol{v}_h) + a_h(\boldsymbol{u}_h,\boldsymbol{v}_h) + b_h(\boldsymbol{v}_h,p_h) \\ &- b_h(\boldsymbol{u}_h,q_h) + \alpha_3 j(p_h,q_h). \end{aligned}$$

We have the following theorem.

THEOREM 5.1. *Under the conditions of the previous lemma, there exists constant* $h_0 > 0$, $c_5 > 0$, *such that*

$$\sup_{(v_h,q_h)\in\boldsymbol{X}_h\times Q_h^\Gamma}\frac{|A((\boldsymbol{u}_h,p_h),(\boldsymbol{v}_h,q_h))|}{|||(\boldsymbol{v}_h,q_h)|||_h} \ge c_5\, |||\,(\boldsymbol{u}_h,p_h)|||_h,$$

for all $(\boldsymbol{u}_h,p_h)\in\boldsymbol{X}_h\times Q_h^\Gamma$.

Proof. For any given $(\boldsymbol{u}_h,p_h)\in\boldsymbol{X}_h\times Q_h^\Gamma$, by Lemma 5.1, we could choose a function $\boldsymbol{w}_h\in\boldsymbol{X}_h$ such that

$$\frac{b(\boldsymbol{w}_h,p_h)}{\|\boldsymbol{w}_h\|_h} \ge c_1\|\mu^{-\frac{1}{2}}p_h\|_{0,\Omega_{1,h}\cup\Omega_{2,h}} - c_2\frac{j(p_h,p_h)}{\|\mu^{-\frac{1}{2}}p_h\|_{0,\Omega_{1,h}\cup\Omega_{2,h}}}.$$

Then rescale $\boldsymbol{w_h}$ by a constant still denote it as $\boldsymbol{w_h}$ so that $\|\boldsymbol{w}_h\|_h = \|\mu^{-\frac{1}{2}}p_h\|_{0,\Omega_{1,h}\cup\Omega_{2,h}}$. Then we have

$$b(\boldsymbol{w}_h,p_h) \ge c_1\|\mu^{-\frac{1}{2}}p_h\|^2_{0,\Omega_{1,h}\cup\Omega_{2,h}} - c_2 j(p_h,p_h).$$

Take $\boldsymbol{v}_h = \boldsymbol{u}_h + \delta w_h$, and $q_h = p_h$, then we have

$$\begin{aligned} &A((\boldsymbol{u}_h,p_h),(\boldsymbol{v}_h,q_h)) \\ =& \alpha_0 m(\boldsymbol{u}_h,\boldsymbol{u}_h) + \alpha_0\delta m(\boldsymbol{u}_h,\boldsymbol{w}_h) + \delta c_h(\boldsymbol{u}_h^{n-1};\boldsymbol{u}_h,\boldsymbol{w}_h) + a_h(\boldsymbol{u}_h,\boldsymbol{u}_h) + \delta a_h(\boldsymbol{u}_h,\boldsymbol{w}_h) \\ &+\delta b_h(\boldsymbol{w}_h,p_h) + \alpha_3 j(p_h,p_h) \\ \ge& \|\boldsymbol{u}_h\|_h^2 - \delta c_3\|\boldsymbol{u}_h\|_h\|\boldsymbol{v}_h\|_h + \delta c_1\|\mu^{-\frac{1}{2}}p_h\|^2_{0,\Omega_{1,h}\cup\Omega_{2,h}} + (\alpha_3 - c_2\delta)j(p_h,p_h) \\ \ge& \left(1 - \frac{\delta c_3}{2c_1}\right)\|\boldsymbol{u}_h\|_h^2 + \frac{\delta c_1}{2}\|\mu^{-\frac{1}{2}}p_h\|^2_{0,\Omega_{1,h}\cup\Omega_{2,h}} + (\alpha_3 - c_2\delta)j(p_h,p_h) \end{aligned}$$

where we used Lemma 5.2 and 5.3. By a proper choice of δ and α_3, so that $1-\frac{\delta c_3}{2c_1} = \frac{1}{2}$ and $\alpha_3 - c_2\delta \ge 1$, then there exists a proper $C > 0$,

$$A((\boldsymbol{u}_h,p_h),(\boldsymbol{v}_h,q_h)) \ge C\,|||\,(\boldsymbol{u}_h,p_h)\,|||_h^2\,. \qquad ∎$$

Combine this with

$$\|\|(\boldsymbol{v}_h, q_h)\|\|_h^2 = \|\boldsymbol{u}_h + \delta w_h\|_h^2 + \left\|\mu^{-\frac{1}{2}} p_h\right\|_{0,\Omega_{1,h}\cup\Omega_{2,h}}^2 + j(p_h, p_h)$$
$$\leq 2\|\boldsymbol{u}_h\|_h^2 + 3\left\|\mu^{-\frac{1}{2}} p_h\right\|_{0,\Omega_{1,h}\cup\Omega_{2,h}}^2 + j(p_h, p_h).$$
$$= 3\,\|\|\,(\boldsymbol{u}_h, p_h)\|\|_h^2,$$

We finish the proof the theorem.

The above theorem is essential to show the well-posedness of the fully discrete scheme.

THEOREM 5.2. *There exists a unique solution for the decoupled scheme* (4.6)-(4.7).

Proof. By standard arguments [48], the well-posedness of the discrete Oseen equation (4.6) is a direct conclusion of Theorem 5.1 and the continuity of the belinear form $A(\cdot,\cdot)$. The inf-sup condition for SDFEM of the discrete level-set equation can be found in [44] and this makes sure the well-posedness of (4.7). In all, the decoupled scheme is well-posed. ∎

6. Numerical experiments.

In this section, we present some numerical examples to show the efficiency of the method. We will first test the accuracy of the numerical scheme and then present numerical simulations to some interesting two-phase flow problems with MCLs.

6.1. Convergence tests.

We first test the convergence behaviour of the numerical method proposed in Section 4. Here we use the Ren-E model for simplicity in the following two examples. The results for the Cox model and the Onsager model are similar.

Example 1. *Convergence rate for a stationary problem.* In this example, we consider a stationary problem where the solution is known explicitly so that we can compute the errors of the velocity and pressure.

In this examples, we set $\rho_1 = \rho_2 = 1$, $\eta_1 = \eta_2 = 1$ and $\gamma = 1$. We choose the parameters $\beta_1 = \beta_2 = 10^6$, which gives a slip length $l_s = \eta/\beta_i = 10^{-6}$. The other parameters are chosen as $\beta_L = 30$ and the Nitsche parameters $\alpha_1 = \alpha_2 = 30$. The effect of the Nitsche parameter has been studied numerically in [42] and the best results is obtained when it is in $(10, 50)$. We ignore the gravity and assume that the Young's angle is $\theta_Y = 90°$. In equilibrium, the droplet will take a semi-spherical shape. The geometric setup of the example is as follows. We consider a domain $\Omega = (0, 0.5) \times (0, 0.5) \times (0, 0.25)$. The center of the droplet is on the bottom surface with coordinate (0.25,0.25,0). The radius of the droplet is $R = 0.1$. We set the initial conditions $\boldsymbol{u} = 0$ and the initial shape is semi-spherical. Since the initial state is already in equilibrium, we can see that zero is the exact solution for velocity. The pressures in the two fluids are constants denoted as $p^{\pm}$. By the Young-Laplace equation, the pressure difference satisfies $p^- - p^+ = \gamma R$, where p^- and p^+ are respectively the pressures inside the droplet and in the outside fluid. By the condition $\int_\Omega p dx = 0$, we can easily compute the exact solutions for the pressure are

$$p^- = p^+ + \gamma R = \gamma R(|\Omega| - V_0)/|\Omega|,$$

where $|\Omega|$ is the volume of Ω and $V_0 = \frac{2\pi}{3}R^3$ is the volume of the droplet.

We compute the L^2-errors of the velocity and pressure. The results are shown in Table 2. We could see that both the pressure and velocity have a second order convergence rate with respect to mesh size. This is the same for two-phase flows problem without MCLs [47, 44].

Table 2: The convergence rate for velocity and pressure.

Mesh level	velocity		pressure	
	#Err	#Rate	#Err	#Rate
0	2.040E-5	–	1.436E-3	–
1	4.109E-6	2.31	3.889E-4	1.88
2	1.004E-6	2.03	9.714E-5	2.00
3	2.415E-7	2.06	2.384E-5	2.03
4	5.866E-8	2.04	5.796E-6	2.04

Example 2. *Convergence for a dynamic problem.* In this example, we will study the convergence of the method for a dynamic problem. The setup are almost the same as in the previous examples, except the Young's angle. Here we set $\theta_Y = 30°$. We use adaptive meshes to solve the problem. The mesh is refined near the interface of the two-phase flow and h denotes the size of the refined mesh.

Since the semi-spherical shape is not an equilibrium state anymore, the droplet will spread to the equilibrium state. In Figure 2, we show that the numerical results for the problem by using the numerical method presented in Section 4. Since the problem is axis-symmetric, we show only the profile of the droplet in the plane $\{x_1 = 0.25\}$. We see that the nice convergence of the numerical solutions even when the mesh size is much larger than the slip length. The dynamics are almost the same for the three meshes. In comparison, it is known that the numerical solutions may not converge when the mesh size is larger than the slip length (10^{-6} in this example) for standard methods c.f. [26, 35]. This implies that our method has much better convergence property than the standard methods.

6.2. Macroscopic computations. In this subsection we present some numerical experiments by the macroscopic models. We first do some comparisons for the Ren-E model, the Cox model and the Onsager model. Then we do comparison with physical experiments. Finally, we show an example with contact angle hysteresis.

Example 3. *Comparisons for various models.* In this example, we compare different models for MCLs introduced in Section 2. The setup of the numerical experiment is the same as in the previous example. Here we consider three different models for moving contact line, i.e. the Ren-E model, the Cox model and the Onsager model. The numerical results are shown in Figure 3. Here we also show only the intersection of the droplet with the plane $\{x = 0.25\}$. We can see that the dynamics of the droplet computed by the Onsager model is similar to that by the Cox model. However, there exists obvious difference between the numerical results by the Ren-E model and those by the other models. The droplet spreads much faster when we use the Ren-E model. This is easy to understand since there exists extra energy dissipation near the contact line for the two macroscopic models. The macroscopic models should be used for the problem when the characteristic size of the droplet is much larger than the slip length, as discussed [28].

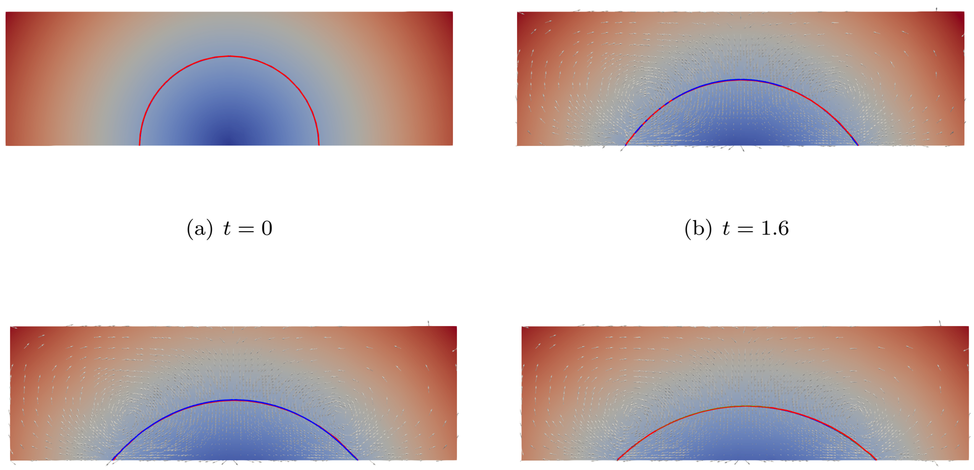

(a) $t = 0$ (b) $t = 1.6$

(c) $t = 2.4$ (d) $t = 4.0$

Figure 2: Shape of a spreading droplet at different time. Red: $h = 1/32$, blue: $h = 1/64$, green: $h = 1/128$. Background color shows the value of the level-set function. The arrows represent the velocity.

Example 4. *Comparison with experiments.* In this example, we use our method to simulate a liquid-liquid displacement problem and compare with the physical experiments in [49]. The experimental setup of the problem is as follows. A water droplet is injected to a n-decane liquid by a glass capillary. The droplet detaches from the capillary and attaches with a flat quartz substrate. Due to gravity and the wetting properties, the water droplet will spread on the substrate and the profile is captured from the side by a high-speed camera. The spreading radius of the droplet on the substrate is a function of time. The physical parameters are as follows. The density of water is $\rho_1 = 1\text{gcm}^{-3}$ and that of n-decane is $\rho_2 = 0.73\text{gcm}^{-3}$. The viscosity of water and decane are $\mu_1 = 1.0087\text{cP}$ and $\mu_2 = 0.85\text{cP}$, respectively. The interfacial tension of the interface between water and decane is $\gamma = 50.12\text{mN/m}$. The equilibrium Young's angle of the water in decane is $\theta_Y = 58.16^o$. The contact line friction $\xi_m = 0.3072\text{Pa}\cdot\text{s}$.

In our simulations, we choose the above physical parameters without any adjustment. We first do nondimensionalization to the problem (2.1)-(2.3) and (2.12). The characteristic length of the problem is 1mm and the characteristic velocity is chosen to be 1mm/s. The geometric setup of our simulations is as follows. We consider a box $(0, 6) \times (0, 6) \times (0, 3)$. The initial radius droplet is 0.92 with centered as $(3, 3, 0.91)$. We use the Onsager model to do simulations. The initial velocity is $\mathbf{v} = 0$. We compare the spreading radius (as a function of time) with experimental observations and the results are shown in Figure 4. We could see that the simulation results are very close to the experiments. The curves are plotted in a log-log frame. The scaling law of the spreading radius in both simulations and experiments are almost the same with

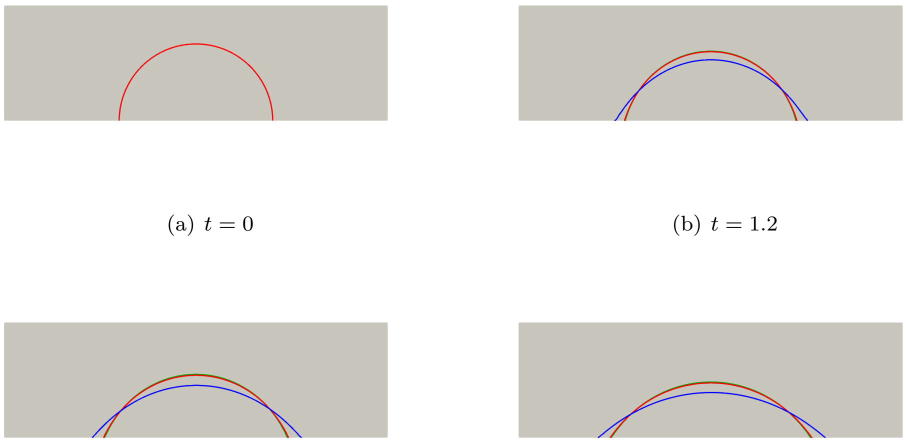

(a) $t = 0$ (b) $t = 1.2$

(c) $t = 2.4$ (d) $t = 4.8$

Figure 3: Shape of a spreading droplet at different time computed by different models. Blue: the Ren-E model; green: the Cox model, red: the Onsager model.

respect to time. The slight discrepancy between the numerical simulations and the experimental results may comes from the fact that the initial states may be different. In physical experiments, the detachment process between the droplet and the capillary may affect the initial dynamics, while in numerical simulations we assume that the droplet slightly attaches with the substrate with zero velocity in the initial state.

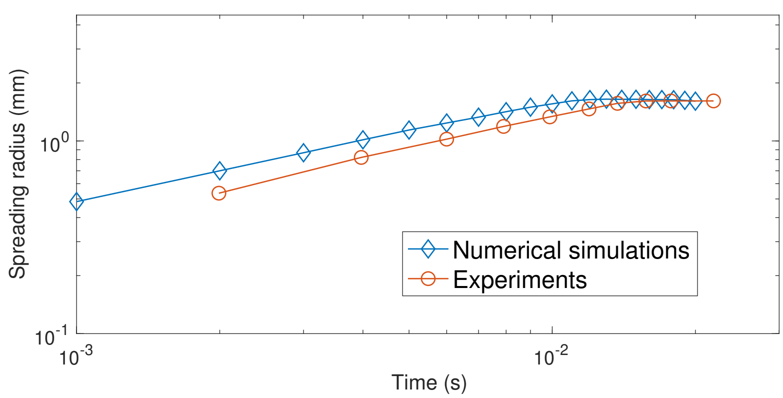

Figure 4: Compare with experimental data

Example 5. (*Simulations for contact angle hysteresis.*) We consider a sliding droplet on a vertical wall with contact angle hysteresis. We set $\eta_1 = \eta_2 = 1$ and $\gamma = 1$. The gravitational acceleration is $\boldsymbol{g} = -9.81\mathbf{e}_3$ and $\beta_1 = \beta_2 = 10^6$, $\beta_L = 0.05$. The constant in Nitsche terms is set to be $\alpha_1 = \alpha_2 = 30$. We choose the CAH model in the simulations and $\theta_Y(z) = \theta_1 + (\theta_2 - \theta_1)(1 + \cos(4\pi z))/2$ with $\theta_1 = 30^o$ and $\theta_2 = 90^o$. The initial shape is a semi-spherical with radius $r = 0.08$ imposed on the left boundary $\{x_2 = 0\}$ of a box $(0, 0.5) \times (0, 0.15) \times (0, 0.5)$. We choose an adaptive mesh and the meshsize near the interface is $h = 1/64$ and set $\Delta t = 0.125$ in numerical experiment.

In the first test, we set $\rho_1 = 5$ and $\rho_2 = 1$. The numerical results are shown in Figure 5. We could see that the initial droplet is a semi-spherical. Then the shape of the droplet changes due to the gravity effect. Finally, the droplet approaches to an equilibrium state and it is pinned on the vertical surfaces. This is due to the existence of the contact angle hysteresis.

In the second test, we change the ratio of the density by setting $\rho_1 = 20$ and $\rho_2 = 1$. The difference between the advancing contact angle and the receding one is the same as in the previous one. The numerical results are shown in Figure 6. We could see that the droplet slides down from the substrate and the shape also changes during the process. There is no equilibrium state in this case since the pinning force can not balance the gravitational force anymore.

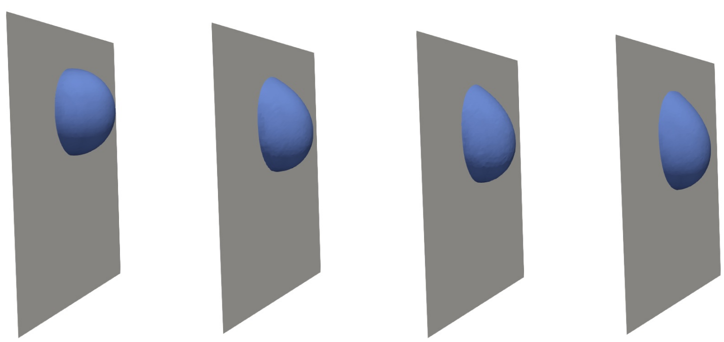

(a) $t = 0$ (b) $t = 2.5$ (c) $t = 5$ (d) $t = 20$

Figure 5: Pinning of a droplet on a vertical wall with CAH

7. Conclusions. In this paper, we propose a unified framework for some important sharp interface models for two-phase flow with moving contact lines. We reformulate the Cox boundary condition and a CAH model and prove them to be thermodynamically consistent. To handle the unbounded parameters in the models, we introduce a new variational form by using the Nitsche technique. This enables us to develop a stable and efficient numerical method independent of the choice the slip length and the contact line friction coefficient. By the method we can solve the Cox type models and the CAH model naturally without resolving the fine scale near the contact line. Overall, this leads to an efficient and reliable numerical framework for macroscopic simulations for the complicated two phase flow problems with MCLs. Numerical experiments show that the method has nice convergence property and can fit with the physical experiments very well even on a relatively coarse mesh.

Theoretically, we show the stability of the numerical method by proving an inf-

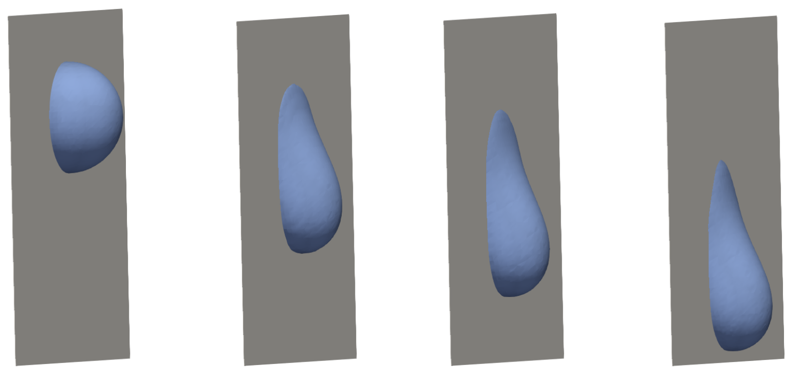

(a) $t = 0$ (b) $t = 10$ (c) $t = 20$ (d) $t = 40$

Figure 6: Sliding of a droplet on a vertical wall with CAH

sup condition which is independent of the choice of the parameters. In the future, we will further do error analysis for the method. This is quite difficult since the flow field and the pressure might be less regular near the contact line [50].

REFERENCES

[1] D. Bonn, J. Eggers, J. Indekeu, J. Meunier, and E. Rolley. Wetting and spreading. Reviews of Modern Physics, 81(2):739, 2009.

[2] J. H. Snoeijer and B. Andreotti. Moving contact lines: scales, regimes, and dynamical transitions. Annual Rev. Fluid Mech., 45:269–292, 2013.

[3] C. Huh and L.E. Scriven. Hydrodynamic model of steady movement of a solid/liquid/fluid contact line. J. colloid Interface Sci., 35(1):85–101, 1971.

[4] J. F. Joanny and P.-G. De Gennes. A model for contact angle hysteresis. J. Chem. Phys., 81(1):552–562, 1984.

[5] P.G. de Gennes, F. Brochard-Wyart, and D. Quere. Capillarity and Wetting Phenomena. Springer Berlin, 2003.

[6] X. Xu and X. P. Wang. Analysis of wetting and contact angle hysteresis on chemically patterned surfaces. SIAM J. Appl. Math., 71:1753–1779, 2011.

[7] LM Hocking. A moving fluid interface. part 2. the removal of the force singularity by a slip flow. Journal of Fluid Mechanics, 79(02):209–229, 1977.

[8] P. Sheng and M. Zhou. Immiscible-fluid displacement: Contact-line dynamics and the velocity-dependent capillary pressure. Phys. Rev. A, 45:5694–5708, 1992.

[9] L. M. Pismen and Y. Pomeau. Disjoining potential and spreading of thin liquid layers in the diffuse-interface model coupled to hydrodynamics. Physical Review E, 62(2):2480, 2000.

[10] T. D Blake. The physics of moving wetting lines. Journal of Colloid and Interface Science, 299(1):1–13, 2006.

[11] T. Qian, X.P. Wang, and P. Sheng. Molecular scale contact line hydrodynamics of immiscible flows. Phys. Rev. E, 68:016306, 2003.

[12] T. Qian, X.P. Wang, and P. Sheng. A variational approach to moving contact line hydrodynamics. J. Fluid Mech., 564:333–360, 2006.

[13] W. Ren and W. E. Boundary conditions for the moving contact line problem. Phys. Fluids, 19(2):022101, 2007.

[14] W. Ren and W. E. Contact line dynamics on heterogeneous surfaces. Phys. Fluids, 23:072103, 2011.

[15] T. D. Blake and J. De Coninck. Dynamics of wetting and kramers's theory. The European Physical Journal Special Topics, 197(1):249–264, 2011.

[16] Y. D. Shikhmurzaev. The moving contact line on a smooth solid surface. Inter. J. Multiphase

Flow, 19(4):589–610, 1993.
[17] Y. D. Shikhmurzaev. Capillary flows with forming interfaces. Chapman and Hall/CRC, 2007.
[18] D. Jacqmin. Contact-line dynamics of a diffuse fluid interface. J. Fluid Mech., 402:57–88, 2000.
[19] P. Yue, C. Zhou, and J. J. Feng. Sharp-interface limit of the Cahn-Hilliard model for moving contact lines. J. Fluid Mech., 645:279–294, 2010.
[20] M. Renardy, Y. Renardy, and J. Li. Numerical simulation of moving contact line problems using a volume-of-fluid method. Journal of Computational Physics, 171(1):243–263, 2001.
[21] P. D.M. Spelt. A level-set approach for simulations of flows with multiple moving contact lines with hysteresis. Journal of Computational Physics, 207(2):389–404, 2005.
[22] M. Gao and X.-P. Wang. A gradient stable scheme for a phase field model for the moving contact line problem. Journal of Computational Physics, 231(4):1372–1386, 2012.
[23] J. Sprittles and Y. Shikhmurzaev. Finite element simulation of dynamic wetting flows as an interface formation process. J. Comp. Phys., 233:34–65, 2013.
[24] J. Urquiza, A. Garon, and M.-I. Farinas. Weak imposition of the slip boundary condition on curved boundaries for Stokes flow. J. Comp. Phys., 256:748–767, 2014.
[25] J. Shen, X. Yang, and H. Yu. Efficient energy stable numerical schemes for a phase field moving contact line model. Journal of Computational Physics, 284:617–630, 2015.
[26] A. Reusken, X. Xu, and L. Zhang. Finite element methods for a class of continuum models for immiscible flows with moving contact lines. International Journal for Numerical Methods in Fluids, 84:268–291, 2017.
[27] Y. Sui, H. Ding, and P. Spelt. Numerical simulations of flows with moving contact lines. Annual Rev. Fluid Mech., 46:97–119, 2014.
[28] Y. Sui and P. D.M. Spelt. An efficient computational model for macroscale simulations of moving contact lines. J. Comp. Phys., 242:37–52, 2013.
[29] Y. Sui and P. D. Spelt. Validation and modification of asymptotic analysis of slow and rapid droplet spreading by numerical simulation. Journal of Fluid Mechanics, 715:283–313, 2013.
[30] R. Cox. The dynamics of the spreading of liquids on a solid surface. Part 1. Viscous flow. J. Fluid Mech., 168:169–194, 1986.
[31] R.G. Cox. Inertial and viscous effects on dynamic contact angles. Journal of Fluid Mechanics, 357:249–278, 1998.
[32] S. Afkhami, S. Zaleski, and M. Bussmann. A mesh-dependent model for applying dynamic contact angles to VOF simulations. J. of Fluid Mech., J. Comp. Phys.:5370–5389, 2009.
[33] Z. Solomenko, P. D.M. Spelt, and P. Alix. A level-set method for large-scale simulations of three-dimensional flows with moving contact lines. Journal of Computational Physics, 348:151–170, 2017.
[34] J.-B. Dupont and D. Legendre. Numerical simulation of static and sliding drop with contact angle hysteresis. Journal of Computational Physics, 229(7):2453–2478, 2010.
[35] J. Zhang and P. Yue. A level-set method for moving contact lines with contact angle hysteresis. Journal of Computational Physics, page 109636, 2020.
[36] P. Yue. Thermodynamically consistent phase-field modelling of contact angle hysteresis. Journal of Fluid Mechanics, 899, 2020.
[37] Z. Zhang and X. Xu. Effective boundary conditions for dynamic contact angle hysteresis on chemically inhomogeneous surfaces. Journal of Fluid Mechanics, 935, 2022.
[38] S. Xiao, X. Xu, and Z. Zhang. Multiscale analysis for dynamic contact angle hyeteresis on rough surfaces. to apear in SIAM Multi. Mod. Simul., 2023.
[39] D. Guan, Y. Wang, E. Charlaix, and P. Tong. Asymmetric and speed-dependent capillary force hysteresis and relaxation of a suddenly stopped moving contact line. Phys. Rev. Lett., 116(6):066102, 2016.
[40] D. Guan, Y. Wang, E. Charlaix, and P. Tong. Simultaneous observation of asymmetric speed-dependent capillary force hysteresis and slow relaxation of a suddenly stopped moving contact line. Phys. Rev. E, 94(4):042802, 2016.
[41] M. Juntunen and R. Stenberg. Nitsche's method for general boundary conditions. Mathematics of computation, 78(267):1353–1374, 2009.
[42] M. Winter, B. Schott, A Massing, and W. A. Wall. A nitsche cut finite element method for the oseen problem with general navier boundary conditions. Computer Methods in Applied Mechanics and Engineering, 330:220–252, 2018.
[43] S. Guo, M. Gao, X. Xiong, Y. J. Wang, X.-P. Wang, P. Sheng, and P. Tong. Direct measurement of friction of a fluctuating contact line. Physical Review Letters, 111(2):026101, 2013.
[44] S. Gross and A. Reusken. Numerical methods for two-phase incompressible flows, volume 40. Springer Science & Business Media, 2011.
[45] P. Hansbo, M. G. Larson, and S. Zahedi. A cut finite element method for a stokes interface problem. Applied Numerical Mathematics, 85:90–114, 2014.

[46] A. Reusken. Analysis of an extended pressure finite element space for two-phase incompressible flows. Computing and visualization in science, 11(4):293–305, 2008.
[47] M. Kirchhart, S. Gross, and A. Reusken. Analysis of an xfem discretization for stokes interface problems. SIAM Journal on Scientific Computing, 38(2):A1019–A1043, 2016.
[48] A. Ern and J.-L. Guermond. Theory and practice of finite elements, volume 159. Springer, 2004.
[49] W Zheng, B. Wen, C. Sun, and B. Bai. Effects of surface wettability on contact line motion in liquid–liquid displacement. Physics of Fluids, 33(8):082101, 2021.
[50] Y. Guo and I. Tice. Stability of contact lines in fluids: 2d stokes flow. Archive for Rational Mechanics and Analysis, 227(2):767–854, 2018.